LA-UR-01-1415
Approved for public release; distribution is unlimited.

Title: **Estimation of relativistic accretion disk parameters from iron line emission**

Author(s): V. I. Pariev, B. C. Bromley and W. A. Miller

Submitted to:

http://lib-www.lanl.gov/la-pubs/00796055.pdf

Estimation of relativistic accretion disk parameters from iron line emission

V. I. Pariev[1,2]
Theoretical Astrophysics Group, T-6, MS B288, Los Alamos National Laboratory, Los Alamos, NM 87545

B. C. Bromley
Department of Physics, The University of Utah, 201 James Fletcher Bldg, Salt Lake City, Utah 84112

W. A. Miller
Theoretical Astrophysics Group, T-6, MS B288, Los Alamos National Laboratory, Los Alamos, NM 87545

ABSTRACT

The observed iron Kα fluorescence lines in Seyfert I galaxies provide strong evidence for an accretion disk near a supermassive black hole as a source of the emission. Here we present an analysis of the geometrical and kinematic properties of the disk based on the extreme frequency shifts of a line profile as determined by measurable flux in both the red and blue wings. The edges of the line are insensitive to the distribution of the X-ray flux over the disk, and hence provide a robust alternative to profile fitting of disk parameters. Our approach yields new, strong bounds on the inclination angle of the disk and the location of the emitting region. We apply our method to interpret observational data from MCG-6-30-15 and find that the commonly assumed inclination 30° for the accretion disk in MCG-6-30-15 is inconsistent with the position of the blue edge of the line at a 3σ level. A thick turbulent disk model or the presence of highly ionized iron may reconcile the bounds on inclination from the line edges with the full line profile fits based on simple, geometrically thin disk models. The bounds on the innermost radius of disk emission indicate that the black hole in MCG-6-30-15 is rotating faster than 30 % of theoretical maximum. When applied to data from NGC 4151, our method gives bounds on the inclination angle of the X-ray emitting inner disk of $50 \pm 10°$, consistent with the presence of an ionization cone grazing the disk as proposed by Pedlar et al. (1993). The frequency extrema analysis also provides limits to the innermost disk radius in another Seyfert 1 galaxy, NGC 3516, and is suggestive of a thick disk model.

Subject headings: accretion, accretion disks — black hole physics — galaxies: active — line: profiles — X-rays: galaxies

1. Introduction

The *Advanced Satellite for Cosmology and Astrophysics* (ASCA) has provided data from over a dozen Seyfert I galaxies to reveal the presence of iron emission lines which are broadened by a considerable fraction of the speed of light — greater than 0.2 c in some cases (Mushotzky et al. 1995; Tanaka et al. 1995; Nandra et al. 1997a). The observed line profiles are the most direct evidence for the presence of

[1]Steward Observatory, University of Arizona, 933 North Cherry Avenue, Tucson, AZ 85721

[2]P. N. Lebedev Physical Institute, Leninsky Prospect 53, Moscow 117924, Russia

supermassive ($\sim 10^8$ $M_\odot$) black holes in the centers of these galaxies: the spectra have distinctive skewed, double-peaked profiles which reflect the Doppler and gravitational shifts associated with emitting material in a strongly curved spacetime (Chen & Halpern 1989; Fabian et al. 1989; Laor 1991; Kojima 1991). The data strongly support a model wherein the emission lines are produced by iron Kα fluorescence at 6.4 keV when optically thick, "cold" regions of an accretion disk (such that the ionization state of iron is less than Fe XVII) are externally illuminated by hard X-rays (George & Fabian 1991; Matt, Perola & Piro 1991). In one bright, well-studied source, MCG-6-30-15, the high signal-to-noise ratio has enabled parameters of a simple geometrically thin, relativistic model to be estimated (Tanaka et al. 1995; Dabrowski et al. 1997; Reynolds, Begelman 1997; Bromley, Miller & Pariev 1998).

The model parameters which may be gleaned from line profiles include disk radii, emissivity of the disk, observed inclination angle of the disk i ($i = 0^\circ$ is face-on and $i = 90^\circ$ is edge-on), and the spin parameter of the black hole, $a_* = Jc/GM^2$, where J is the hole's angular momentum. If the hole is rotating, we assume that the disk lies in the equatorial plane of the black hole, as a result of the Bardeen–Peterson (1975) alignment mechanism, and that the disk is corotating. Of these parameters, perhaps the most problematic is the disk emissivity. The distribution of the hard X-ray flux which illuminates the disk determines the emissivity of the fluorescing disk material, and therefore has a strong influence on line profiles. The emissivity is usually assumed to be axisymmetric. This is reasonable if the observed profile is obtained with a long integration time since strong asymmetries presumably would average out. Specific choices for emissivity include a power-law in radius (Fabian et al. 1989; Bromley, Chen & Miller 1997), a form consistent with a point source of illumination (Matt, Fabian & Ross 1993; Matt, Fabian & Ross 1996; Reynolds & Begelman 1997), and a function proportional to the total energy flux in the Page & Thorne (1974) accretion model (Dabrowski et al. 1997). Dabrowski et al. (1997) also considered a non-parametric form of the emissivity function. Recently, Iwasawa et al. (1999) performed a line-profile fit assuming nonaxisymmtric X-ray illumination of the disk in MCG–6-30-15. Nonaxisymmetric emissivity might be expected for the bright state of this source if the mass of the central black hole is $\sim 10^8\, M_\odot$. In this case the integration time of the observations is shorter than the orbital period at a radius of a few times that of the horizon.

The calculation of emissivity may be complicated somewhat by the local physics of the disk as well as the nature of the illuminating source. If the incident radiation is strong it can cause iron to become highly or fully ionized. For iron atoms at ionization stages no higher than Fe XVI, Kα emission occurs at 6.4 keV, however, resonant absorption and successive Auger processes prevent significant line emission by Fe XVII through Fe XXIII. Lithium– and Helium–like ions, Fe XXIV and Fe XXV, emit at approximately 6.7 keV, while Hydrogen–like ion Fe XXVI produce Kα line at 6.97 keV (Matt et al. 1996; Matt et al. 1993; see also the review by Fabian et al. 2000).

Local anisotropy of rest-frame emission is another effect which can influence an observed line profile. It is often assumed that the emitter is locally isotropic, although Laor (1991) considered limb darkening and Matt et al. (1996) considered effects of resonant absorption and scattering which can result in anisotropic emission.

The next level of detail in modeling local disk physics was to consider non-Keplerian flows, as when material falls within the innermost stable orbit around a Schwarzschild black hole (Reynolds & Begelman 1997), or when there is turbulence in a disk of finite thickness (Pariev & Bromley 1998). More recently, temporal variations in line profiles (Lee et al., 2000; Iwasawa et al., 1999; Nandra et al., 1999) have been observed. Simulations of line profiles with a time-dependent illumination (Reynolds et al. 1999; Young & Reynolds, 2000; Ruszkowski 1999) are also performed. Knowledge of the line variability can provide

information about the size of the inner region of the accretion disk and the mass of a black hole.

To circumvent uncertainties in the emissivity of the disk and yet still obtain estimates and constraints of fundamental disk parameters such as the inner radius, Bromley, Miller & Pariev (1998) suggested using the minimum and maximum frequency shifts of a broad emission line as a diagnostic. As first demonstrated by Cunningham (1975), the edges of a line profile from an emitting disk annulus uniquely determine the radius of the annulus and its inclination. Similarly, bounds may placed on these parameters when the emission comes from many such annuli. These bounds are more robust indicators than estimates derived by fitting the full profile shape when the emissivity is nonaxisymmetric or when the continuum has been poorly modeled in the central regions of the broad lines.

In this work we use the method of line frequency extrema to study the geometric and kinematic properties of relativistic accretion disks. We provide new methods of line edge detection based on polynomial fits to the line profile and continuum, and compare the results to the χ^2 rejection technique used by Bromley, Miller & Pariev (1998). In § 2 we describe the minimum and maximum frequency diagnostic and ways to determine the position of a line edge and its error. In § 3 we apply the technique to the iron line profiles from MCG-6-30-15, NGC 4151, and NGC 3516, and we compare the results of the edge fitting to the fitting of the whole line profile. Finally, we discuss prospects for our method with data from future X-ray missions.

2. The Method of Minimum and Maximum Frequency Shifts

2.1. Description of the Method

The information contained in a line profile is rich, but the parameter space of models is also fairly large. Here, as in Bromley, Miller & Pariev (1998), we sacrifice detailed modeling for broad characteristics of the accretion disk by examining only the edges of the line. The gain is a reduced dependence on unrealistic model assumptions such as axisymmetric emissivity or the behavior of the continuum emission over the entire frequency range of the line. For example, the usual continuum model is a power law in frequency, but there is evidence from Iwasawa et al. (1996) that the index can vary in time. Since the lines are extraordinarily broad, one risks the possibility of a poor guess for the continuum which would affect the shape of the inferred profile. This in turn can affect inferences of the disk model parameters, including inner and outer radii. Worse, the profile might also be misinterpreted because our assumptions of axisymmetry might be incorrect, a possibility which is worrisome in light of time variability of the continuum and line profile. For example, patchy, local flares would violate axisymmetry unless the observed line profile were integrated over a long period of time.

From Cunningham (1975), it is clear that minimum and maximum frequency shifts of a line profile themselves contain information about fundamental disk parameters, regardless of details which may complicate the shape of the profile. Here we use the frequency extrema diagnostic for both standard infinitesimally thin disk case and for the disk model taking into account turbulent broadening and additional frequency shifts of the line due to Doppler effect associated with the accretion inflow and correction to the gravitational redshift because of the elevation of the line emitting spots above the equatorial plane of the disk. For the latter case we use results by Pariev & Bromley (1998) for the line profiles emitted from the surface of the "standard" α-disk (Novikov & Thorne 1973). The parameters which uniquely define the system of black hole and accretion disk are the mass of the black hole M, spin parameter of the black hole a_*, and inclination of the disk relative to the observer i. The shape of a time-independent line profile

cannot provide us with the absolute scale of the system, GM/c^2, although variable features in the profile can indicate the black hole mass. In the present work we deal only with time-averaged observations, hence the mass M enters only as degenerate scale factor with disk radius. In the case of the Shakura & Sunyaev (1973) α-disk model, additional model parameters include the luminosity of the disk in Eddington units, $L/L_{\rm ed}$, and a viscosity parameter α. Of course, with fixed values for these parameters, an observation of the luminosity can constrain the black hole mass.

Here we first define $g_{\rm min} = \nu_{\rm min}/\nu_e$ and $g_{\rm max} = \nu_{\rm max}/\nu_e$ to be the minimum and maximum frequency shifts of a line relative to the rest-frame frequency. Then we consider emission from an infinitesimal annulus of the disk with Boyer-Lindquist radius r. For a given value of the spin parameter a_* (as well as luminosity L and viscosity parameter α for a thick disk) there exists a unique mapping $g_{\rm min} = g_{\rm min}(r,i)$, and $g_{\rm max} = g_{\rm max}(r,i)$, connecting frequency extrema of a line and the inclination angle i and radius r of the annulus. An example of such a mapping is given in Figure 1. Note that we use units of gravitational radius, $R_g = GM/c^2$, so that for a nonrotating black hole the radius of event horizon is $2R_g$, and the radius of the innermost stable orbit is $6R_g$; for the maximally rotating astrophysical black hole with $a_* = 0.998$ (Thorne 1974), the radius of the event horizon decreases to $1.063R_g$ and the accretion disk becomes stabilized down to the radius $1.237R_g$. It is this extension of the stable disk down to small radii which is the most prominent effect of rotation of the black hole.

Emission in an observed line consists of the sum of contributions from many infinitesimal annuli. These annuli produce a curve in the $g_{\rm min}$–$g_{\rm max}$ plane, which corresponds to a single, constant inclination angle i. Of course a measured profile will generate a single point in this plane which is simply the extreme values of redshift and blueshift along a constant-i curve. The position of the measured point in the $g_{\rm min}$–$g_{\rm max}$ diagram indicates that emission can come only from the quadrant of the $g_{\rm min}$–$g_{\rm max}$ plane defined by inequalities $g(i,r) > g_{\rm min}$ and $g(i,r) < g_{\rm max}$. At the same time, some emission must come from the points on both sides of this quadrant, i.e. from the points having either $g(i,r) = g_{\rm min}$ or $g(i,r) = g_{\rm max}$. The position of this point can fix the range of possible disk inclination angles i: Since $g_{\rm min}$ increases with increasing r along the curve $i =$ constant, the upper limit on inclination angle of the disk is given by the value of i for the curve $i =$ constant passing through the data point. The lower limit is provided by the $i =$ constant curve which just touches the horizontal line $g = g_{\rm max}$. If $g_{\rm max} < 1$, then the lower limit for i is 0. Furthermore, for each i within the observed bounds one can determine the outer $r_{\rm out}(i)$ and inner $r_{\rm in}(i)$ radii of annulus, which give a contribution to the observed profile. Generally, the middle regions of the disk can have arbitrary amounts of iron line emission, but there must always be some emission coming from points of the disk surface at radii $r = r_{\rm out}(i)$ and $r = r_{\rm in}(i)$.

If several line profiles are available for the same object in different phases of emissivity, then we may be able to place further constraints on the inclination angle of the disk and to check the validity of the accretion disk model (i.e. that bounds for i are not mutually exclusive). Narrower limits for i put tighter constrains on $r_{\rm in}$ and $r_{\rm out}$. We emphasize that these constraints are independent of the emissivity law across the disk.

As mentioned above, by looking only at the position of the edges of line profiles we clearly lose a large amount of the information contained in the shape of a line profile. We instead obtain very strong bounds on the inner radius and inclination angle of the disk. In the case of time variability over time scales not resolved during photon counts integration time, positions of the frequency extrema are still able to provide estimates of the inclination angle of the disk and bounds for the inner edge of the disk. This is an important feature when there are changes in the disk illumination and/or possible obscuration of parts of the disk by absorbers (Weaver & Yaqoob 1998) which can substantially alter the main core of the line.

Another advantage of looking only at the positions of the edges of the line is that it circumvents the effects on the line profile of possible resonant absorption of the line photons in the disk corona. As shown by Ruszkowski & Fabian (1999), reasonable assumptions about the velocity field in the corona of the disk suggest that an absorption feature is located slightly redward of 6.4 keV leaving the red and blue edges of the line unaffected. In this case a direct fit of the profile with a standard Keplerian disk model would give poor results. The frequency extrema method does not require detailed models of absorbing corona or occulting cloud, nor is it sensitive to the reflection from a surrounding torus or any other sources of narrow 6.4keV iron line emission except in the rare instances when the disk is observed almost directly face-on and all disk emission is reddened.

2.2. Theoretical $g_{\rm min}$–$g_{\rm max}$ Maps

We used a general purpose ray-tracing code to calculate values of $g_{\rm min}$ and $g_{\rm max}$ for a number of narrow rings and a number of different inclinations i. The code, described by Bromley, Chen & Miller (1997), generates a pixelized image of the accretion disk as would be seen by a distant observer. The observed frequency at each pixel is given by

$$g \equiv \frac{\nu_o}{\nu_e} = \frac{-1}{-\vec{u}\cdot\vec{p}} \tag{1}$$

where subscripts o and e are observer and emitter respectively, $\vec{u}$ is the 4-velocity of the emitter and $\vec{p}$ is the emitted photon's 4-momentum. Note that the emitter 4-velocity is specified by the disk model, while the photon 4-momentum is calculated by numerically tracing the photon geodesic back in time from the pixel in the observer's sky plane to the surface of the disk. Then, we sort pixels into narrow rings and determine extrema of g over all pixels fallen into a ring between r and $r+\delta r$. To create a grid of lines $i=$ constant and $r=$ constant on $g_{\rm min}$–$g_{\rm max}$ plane we use cubic spline interpolation.

The ray tracer itself is a general-purpose second-order geodesic solver for a Kerr geometry. An arbitrary disk surface can be specified so that the photon trajectories terminate on this surface. For axisymmetric geometries the number of individual geodesics which need to be traced numerically in order to produce complete set of images is of the same order as in the method of transfer functions by Laor (1991). Using of parallel supercomputer allowed us to compute an image of 1000×1000 pixels during about 1 minute of run-time.

Details about modeling the emitter 4-velocity, $\vec{u}$ in equation (1), can be found in Pariev & Bromley (1998). Here, we assume that outside of the orbit of marginal stability the bulk emitter 4-velocity is the sum of a Keplerian 4-velocity and a small, inward radial velocity component as given by Novikov & Thorne (1973). We do not take into account the θ component of inflow velocity, nor the dependence of ϕ component of velocity on the height of the disk. These are higher order corrections to radially directed inflow. Inside of the marginal stability radius, all orbits are presumed to be in free-fall in the equatorial plane with integrals of motion equal to the values at the innermost stable orbit. We assume a simple model for turbulent motion in the disk, with an isotropic Gaussian distribution of turbulent velocities with the square mean equal to the square of the speed of sound c_s^2 averaged over the disk thickness, namely

$$I(\nu_e,\nu,\mu_e,r_e) = \epsilon(r_e,\mu_e)\sqrt{\frac{3}{2\pi}}\frac{c}{c_s}\exp\left[-\frac{3c^2}{2c_s^2}\frac{(\nu-\nu_e)^2}{\nu_e^2}\right]\frac{1}{\nu_e}, \tag{2}$$

where the intensity I at a specified frequency ν depends upon the rest frame energy of the $K\alpha$ line ($\nu_e = 6.4\,{\rm keV}$), the angle cosine μ_e of the photon emission with respect to the normal of the disk as

measured in the source frame, and the radial coordinate r_e of the emitting material on the surface of the disk; $\epsilon(r_e, \mu_e)$ is the surface emissivity; $c_s(r_e)$ is the sound speed at the radius of emission, r_e. We consider only the case of isotropic emission, when $\epsilon = \epsilon(r_e)$. The width of a Gaussian line profile in the comoving frame with the disk surface is $\sigma(r_e) = c_s(r_e)/\sqrt{3}$. The sound speed at a radius r_e is proportional to the accretion rate and, therefore, to the luminosity of the disk (Shakura & Sunyaev 1973; Novikov & Thorne 1973; equation [15] in Pariev & Bromley 1998). Therefore, the amount of smearing of the line at a given radius is proportional to $L/L_{\rm ed}$. Note, that the actual turbulent velocities may have a mean value less than the speed of sound (see Pariev & Bromley 1998 for details), thus we are considering the maximum possible effect of turbulence on line profiles.

Turbulent broadening causes the whole line profile to be smoothed. Particularly, blue and red edges are no longer sharp but have wings of the order of c_s/c at the radii where the edges of the profile are formed. Accretion inflow causes a slight shift of the profile to the red, but does not strongly influence the position of the profile edges, since the edges are formed in regions of the disk which have radial inflow velocities nearly perpendicular to the light ray emerging toward the position of the observer.

Adding a Gaussian turbulent velocity spectrum makes the determination of edges of a theoretical line profile somewhat uncertain. Moreover, the observed extent of a line depends upon the signal–to–noise ratio of the observational data. Keeping in mind that our Gaussian prescription for turbulent broadening is crude and velocities of turbulent motions along line of sight cannot exceed the speed of sound, we assume the following procedure for finding the minimum and maximum redshifts in the case of a turbulent disk model with finite thickness and accretion inflow: We add the value of $\sqrt{3}\sigma(r)/c = c_s(r)/c$ to the uncorrected g_{max} in order to obtain $g_{\rm max}$ and subtract the value of $c_s(r)/c$ from the uncorrected $g_{\rm min}$ in order to obtain $g_{\rm min}$. This procedure is also consistent with a signal–to–noise ratio of about 10% in currently available observational data for line profiles. The grid of $g_{\rm min}$–$g_{\rm max}$ obtained in this way was used in all estimates of parameters of thick disk model and is shown by dashed lines in Figs. 1 and 4 for nonrotating and extremely ($a_* = 0.998$) rotating black holes. To determine the greatest possible effect of the physical structure of the disk, we have chosen a high disk luminosity, $L = L_{\rm ed}$, and an α viscosity parameter of 0.3. These values still consistent with an optically thick disk.

The main effect kinematics and finite disk thickness is to yield larger values for $g_{\rm max}$ and smaller values for $g_{\rm min}$. For a nonrotating black hole the disk extends down to $6R_g$, at which point the thickness of the disk as well as radial inflow velocity approach zero, while the surface density increases without bound (Novikov & Thorne 1973) — this is a consequence of the zero-torque boundary condition at the inner edge of the disk. Thus the difference between the thin and thick disk models vanishes at $6R_g$. In reality, the gas smoothly transits near $6R_g$ from a slow inward spiral caused by viscous stresses to a plunging geodesic orbit into the black hole. Nonzero viscous torque and radial inflow should also change the parameters of the disk just beyond the $6R_g$ orbit (e.g. Beloborodov, Abramowicz & Novikov, 1997). Thus, the shape of the dashed curves in Fig. 1 for $r \leq 10R_g$ should be altered for more realistic situations so that the transition from $r > 6R_g$ to $r < 6R_g$ is smoothed out and dashed lines should move upward and to the left near the $r = 6R_g$ curve of the thin disk model.

Agol & Krolik (2000) consider thin-disk structure when there is a finite time-steady torque on the inner edge of the disk. According to them, additional dissipation near innermost edge of the disk due to the applied torque would cause increased heating and increased sound speed compared to Novikov-Thorne disk. Larger sound speed causes dashed lines on Fig. 1 to move upward and to the left. However, Paczynski (2000) points out that any torque at the innermost stable circular orbit should be small as soon as the disk is thin and $\alpha \ll 1$. The subject of the transition from nearly Keplerian flow to rapid infall to the black hole

is under active investigation (e.g., Gammie 1999). We only mention that our method of line frequency extrema diagnostic could be used to put constrains on models resulting from such investigations, but this is beyond the scope of the present work.

The deviation of frequency extrema plots for disks of finite thickness from those for infinitely thin disks scales as $\propto L/L_{\rm ed}$ with the total thermal luminosity of the disk L, while the exact value of the α parameter is not nearly as important (Pariev & Bromley, 1998). When then accretion rate and the ratio $L/L_{\rm ed}$ decrease, the sound speed, radial inflow velocity and thickness of the disk also decrease. In the limit of very small accretion rates and very small $L/L_{\rm ed}$, the solid and dashed grids in Fig. 1 and Fig. 4 becomes coincident. For very low accretion rates the disk can be regarded as thin, with each light-emitting element moving on a circular Keplerian trajectory with little turbulent broadening.

2.3. Line Blending

Blending of emission lines having different rest-frame frequencies would influence results of using frequency extrema method. The most important sources of blending can be the presence of Kα emission from highly ionized iron, emission of iron Kβ at 7.06 keV, and nickel Kα 7.48 keV line (George & Fabian 1991). The most difficult to estimate is the contribution of the hot (i.e., highly ionized) iron Kα line. Hot disks can fluoresce in the Kα line under certain circumstances, depending on the three-dimensional temperature structure of the disk. These issues were given consideration by Matt et al. (1996), Matt et al. (1993), and Życki & Czerny (1994): The basic conclusion reached by these authors is that the rest-frame frequency, intensity, and angular dependence of the emission are determined by the value of the ionization parameter $\xi(r) = 4\pi F_X(r)/n_{\rm H}$, where $F_X(r)$ is the X-ray illuminating power-law flux striking a unit area of the disk surface, and $n_{\rm H}$ is a comoving hydrogen number density. In order to determine ξ one must know the characteristics of the source of illuminating X-rays such as its intensity, spatial distribution, and motion relative to the disk. Some aspects of the dependence of the line profile and equivalent width on these characteristics have been outlined in Reynolds & Begelman (1997) and Reynolds & Fabian (1997). Our estimate of the parameter ξ along the lines described in Reynolds & Begelman (1997) shows that for a thin α–disk around a Schwarzschild black hole it can plausibly lie either above or below the threshold value for ionization $200\,{\rm erg\,cm\,s^{-1}}$, depending upon X-ray efficiency of the illuminating source and its spectral index. For the Kerr case when the disk extends close to the event horizon, relativistic aberrations of the illuminating radiation due to gravity, frame dragging, and the motion of material in the disk become very significant, generally leading to the enhancement of the irradiating flux as measured in the comoving frame of the disk material. Consequently, the parts of the disk at small radii are more likely to emit hot iron lines 6.67 keV and 6.97 keV. However, due to resonant scattering and Auger processes, little line emission is produced in the transition region from cold to hot iron lines.

Furthermore, in regions where lines can form, X-ray flares above the disk can cause higher ionization of the disk surface directly below the flare than the rest of the disk. All this makes the analysis of the iron line profile complicated and dependent upon unknown positions of illuminating X-ray sources, accretion rates and mass of the central black hole. We assume that the iron Kα line has 6.4 keV rest frame energy everywhere in the accretion disk. For all observational data considered here, the core of the line is centered close to 6.4 keV, while higher energies for the core can be ruled out with very large degree of confidence. This means that parts of the disk not very close to the black hole ($> 20GM/c^2$), where the core of the line is formed, produce the cold iron 6.4 keV line. One is not so certain about inner parts of the disk producing the red tail of the line, but we assume that the Kα line has the rest frame energy of 6.4 keV throughout

the disk. The maximum possible error in finding $g_{\rm min}$ introduced by this assumption is 0.09, which in most cases is no more than the size of 2σ error box for the values of $g_{\rm min}$ for the present quality of X-ray observations.

Since the Kβ 7.06 keV line is emitted by the same iron atoms that are responsible for the Kα line, the shape of the two profiles should be the same. The ratio of fluorescent yields in Kβ and Kα lines is 0.113 (George & Fabian 1991). If one makes the reasonable assumption that nickel is distributed over the disk surface in the same way as iron, then the profile of nickel Kα line will be similar to that of iron, but shifted by 1.08 keV. The relative abundance of nickel with respect to iron is not known precisely for observed sources but a reasonable value is about 0.06 (George & Fabian 1991).

The fact that the iron Kβ line and the nickel Kα line are faint compared to iron Kα allows us to perform an effective decomposition of the blended profile into the sum of individual profiles of three lines. If $f_{\rm obs}(\nu)$ is the observed excess of photon counts per second over the fitted continuum, and $f(\nu)$ is the actual profile of iron Kα line, then one has the relation

$$f_{\rm obs}(\nu) = f(\nu) + 0.113 f(\nu - 0.64) + 0.06 f(\nu - 1.08).$$

Here we will use the term "energy-corrected profile" for the function f. One can solve this equation for f iteratively, feeding approximations to the function for the contributions from the Kβ and nickel lines. As an initial guess, we take $f_{\rm obs}$ and each subsequent approximation f_{k+1} is obtained using previous values of f_k:

$$f_{k+1}(\nu) = f_{\rm obs}(\nu) - 0.113 f_k(\nu - 0.64) - 0.06 f_k(\nu - 1.08).$$

The actual data points are the integrals of a continuous energy distribution within energy bins. The accuracy in determining $f(\nu)$, which we need according to the quality of the data, is of the order of a few per cent. Therefore, it is sufficient for our purposes to treat data points just as a discrete samples of the underlying continuous function. We computed values of $f_{k+1}(\nu)$ at the center of each energy bin, linearly interpolating between bins to obtain values of $f_k(\nu - 0.64)$ and $f_k(\nu - 1.08)$. When the shifted frequency went beyond the red boundary of the observed data, we used a value of zero for the shifted profile. For the data considered here, the iteration procedure converged with sufficient accuracy in only two iterations.

The main effect of the blending correction is to suppress the blue wing of the line or perhaps create an "absorption" feature if the blue wing is weak or absent. We compared results of determining $g_{\rm max}$ using uncorrected and energy-corrected profiles for the same observation, we found that only in the data with the highest signal-to-noise was there a difference in the detected edge position of greater than 2σ. Thus, at the quality of present X-ray spectral data for most Seyfert galaxies, the corrections for blending with lines other than iron Kα line are small.

2.4. Edge Detection

We are interested in the determining boundary between the line and continuum, not the full profile shape, and we now argue that we can work with the observed counts directly without restoring actual X-ray fluxes by deconvolving with the response matrix of the X-ray detector. All the data considered below were obtained with the ASCA SIS detector; its sensitivity to a monochromatic line varies by a factor of five over the 3-8 keV waveband, with the response function broadening the signal by about 100 eV. One or two satellite peaks also appear at a level not exceeding 3% of the intensity of the main line. The frequency of the satellite peak is about two thirds that of the initial line. In addition, the monochromatic line produces

a small continuous response in each channel with counts less than 1% of the counts in the channel at the peak. The magnitudes of detector response effects are well within the errors of the observed intensity of the line and the spread over 100 eV is comparable to smallest standard error in the position of the edges measured here (see Tables 1 and 2 with the results for edges). Thus, we conclude that folding the broad line and continuum spectrum through the detector response matrix does not have significant (i.e. more than one standard error) influence on the locations of the line edges.

To locate the edge of a line profile, we start with an unconvolved, continuum-subtracted, energy-corrected line profile as observed in the restframe of the host galaxy (i.e., cosmological redshift has been removed). The continuum subtraction was performed differently by different observers: Iwasawa et al. (1996) performed a fit with a single power law absorbed by the Galactic column density ($N_H \approx 4 \times 10^{20}\,\mathrm{cm}^{-2}$) of the underlying continuum in 3-10 keV range for MCG-6-30-15. Iwasawa et al. (1999) slightly improved the continuum fit by adding a reflection component modeled by `pexrav` task (Magdziarz & Zdziarski 1995). However, this reflection component affects line flux by only about 5 per cent. Wang et al. (1999) fitted the continuum in the 1.0–4.0 and 8.0–10.0 keV band with a model which consists of a dual absorbed power law with some fraction (about 5 per cent) of the direct continuum scattered into our line of sight and absorbed only by the Galactic column. Compton reflection was not included in this fit since there is no reliable indication of the existence of the reflection in this object. Nandra et al. (1999) fitted the continuum in the 3.0–4.0 and 7.0–10.0 keV range by a single power law only.

We need to examine only sections of the profile containing a suspected line edge and fit the profile with a linear, polynomial model $y = a_0 + a_1 x + a_2 x^2 + a_3 x^3$ in frequency x. In most instances, a quadratic fit gives the best results, since the cubic term added artificial oscillations to the fit. A linear χ^2 method determines the polynomial coefficients a_i, and these in turn provide roots of the polynomial model. The real root (if it exists) which is closest to the center of the line is taken as the position of the edge.

To estimate the error in measuring the energy of the edge of the line using the roots of a best-fit polynomial we use Monte-Carlo realizations of the observed counts: Each profile consists of a number of counts y_i in energy channels spanning the intervals from $x_i - \Delta_i$ to $x_i + \Delta_i$, where x_i are the central energies of each channel number i, Δ_i are half–widths of the channels. The half–widths of the channels increase with increasing energy and range from about 50 eV at 3 keV to about 700 eV at 9 keV. For each real observed profile we create 20000 artificial data sets by randomly drawing a flux value y from a Gaussian distribution with mean y_i and variance equal to the width of y-error bar σ_i. Then we perform a χ^2 minimization of each artificial data set to get the best-fit polynomials and their roots. Repeating this procedure for all 20000 Monte-Carlo data sets allows us to construct a probability distribution for the location of the line edges determined in this way. Generally, such distributions are skewed with tails extending out from the center of the line. We calculate the mean and the variance of this distribution of edges. Then, we take the mean as the best approximation for the true position of the edge and variance as a standard error of this edge determination. To be more conservative in light of the fact that the distribution of best-fit values is not strictly Gaussian, we take our final values of $g_{\min}$ and $g_{\max}$ to have error boxes twice as large as the standard error given by Monte-Carlo distribution of fits. In most cases, the ellipse in the $g_{\min}$-$g_{\max}$ plane with semimajor axes that are twice the standard errors contain 95% of all roots found.

The results of fitting with the polynomial model are given in Table 1. For the fits we choose only channels on one side of the line peak, either red or blue depending on which edge we are looking for. Each set of channels are continuous in energy and define some interval which brackets a line edge, i.e., the interval contains regions where the spectrum is well-fit to the continuum model as well as channels which exhibit clear and significant signal from line emission. Once chosen, the set of channels remains the same for all fits

in a Monte-Carlo simulation. The actual energy range covered by the fitting intervals varies substantially for different profiles depending on how sharp is the transition from the line to continuum. Roughly, energy range is about 2–3 keV for the red edge and 1–2 keV for the blue edge. Instead of specifying the energy range for each fit we choose to number all points on the plot of the profile and to list those which are used in a particular fit. The points are numbered consecutively with the point number 1 referring to the redmost channel. The numbers of points used in the fits are given in the third column of Table 1.

We also propose a non-linear "sharp edge" model to locate a line edge. In this model the continuum is exactly zero and the line is a linear or quadratic piece which extends from the continuum to higher intensities. At the red edge of a line the model is

$$\begin{aligned} y &= 0 \quad \text{for} \quad x < p_0, \\ y &= p_1(x - p_0) + p_2(x - p_0)^2 \quad \text{for} \quad x > p_0, \end{aligned} \tag{3}$$

while for the blue edge

$$\begin{aligned} y &= 0 \quad \text{for} \quad x > p_0, \\ y &= p_1(x - p_0) + p_2(x - p_0)^2 \quad \text{for} \quad x < p_0, \end{aligned} \tag{4}$$

where in the last case p_1 is negative. The line edge is p_0, the location of the kink which delineates the flat continuum and the regions of increasing flux p_0.

As with the polynomial fitting, we determine the distribution of p_0 in many Monte-Carlo realizations, and take the mean and variance of this distribution as the estimated position of the edge and its corresponding uncertainty. The fitting function (3)-(4) is not smooth and this causes many fits to give p_0 values very close to a mean channel frequency x_i, mimicking a discrete distribution. Therefore, the cumulative distribution of $p_0(x)$ looks like the sum of several step functions. The contour around the mean point $g_{\rm min}$–$g_{\rm max}$ determined from the Monte Carlo simulations which characterizes the scatter in the $g_{\rm min}$–$g_{\rm max}$ simulation points is rectangular in shape rather than the usual ellipse (as in the case of Gaussian distributed $g_{\rm min}$ and $g_{\rm max}$). We verified that for most fits the rectangle, centered on the mean value for the Monte-Carlo simulated $g_{\rm min}$ and $g_{\rm max}$ values and having sides equal to twice the variance of the Monte-Carlo simulations, contains about 95% of fitting points inside it. We plot these 2σ "error-rectangles" as well as best fit to actual data points on the $g_{\rm min}$–$g_{\rm max}$ diagrams in Figs. 4–6. In order to make Figs. 5–6 easier to read, we use asymmetric error bars instead of full "error rectangles." These error bars originate at the point corresponding to the best fit to the actual data. The ends of all four error bar segments define the error rectangle, i.e. the length of each of the four error bars is equal to the distance between best fit point and an edge of the rectangle. All our conclusions about disk geometry assume that the error distributions lie within such rectangles. Table 2 shows edge estimates based on this non-linear model, analogous to Table 1.

In order to verify that the non-linear model gives reasonable determinations of the positions of the line edges we applied the same Monte-Carlo method for finding the edge of an artificial line profile. This mock line profile was created from a real profile in the following way. Starting with the same energy channels $x_i \pm \Delta_i$ as for the real data set, we find the best fit of the non-linear model to the actual data set $y(x)$ and take values of $y(x_i)$ of this fit. Then, using error values corresponding to the real data we apply the same Monte-Carlo procedure of finding the edge of the artificial data set and thus determine the distribution of the parameter p_0. Generally, we obtain the smaller errors and lower χ^2 for this type of fit, while the one standard error intervals for p_0 found by both Monte-Carlo simulations are overlapping (see few exceptions for poor quality edges below). This result is expected since the most likely profile for the data is the actual

measured points, while the most likely profile for any given Monte Carlo realization is the underlying model profile.

Which model, polynomial or non-linear, better approximates the true shape of observed profile? Theoretically one expects that the profile formed by a thin Keplerian disk has sharp edges. Let us consider the part of the disk surface near the innermost edge of the disk, where the reddest photons near the red edge of the line with frequencies from $g_{\min}$ to $g_{\min} + \Delta g$ are emitted. This part of the disk has the shape of the crescent elongated along the inner edge of the disk (e.g., Fig. 8 in Luminet 1979, or color figures in Bromley et al. 1997; Pariev & Bromley 1998). It is easy to see that the area of this crescent is $\propto \Delta g^{3/2}$. Therefore, the flux (or photon counts) per unit frequency near the red edge of the line should be $F_\nu \propto \Delta g^{1/2}$ (if the illumination intensity does not approach zero at the inner edge of the disk). Certainly, the coefficient in these proportionalities gets very small for rapidly rotating black holes because of the large gravitational redshift close to the event horizon and strong relativistic decrease of the intensity of the emitted X-rays. The whole area of the disk, where the red edge of the line is formed ($\sim R_g^2$), is also small. The part of the disk forming the bluest photons has an elliptic shape centered at a point far from the event horizon. Similar consideration for the blue edge of the line gives $F_\nu \propto \Delta g$. However, the coefficient here is large, because the region on the disk surface producing the bluest photons is relatively large. It is for this reason that observed line profiles show much sharper, well-defined blue edges. Sharp red edges can be noticed only for slowly rotating black holes but become less prominent for rotating black holes. Indeed, line profiles for a Schwarzschild system, calculated with high resolution, have a much more distinctive sharp red edge (e.g., Fig. 5 in Pariev & Bromley 1998) than in the case of an extreme Kerr metric. (e.g., Fig. 6 in Pariev & Bromley 1998).

While polynomial fitting does not take into account the theoretically expected shape of the edge profile, the nonlinear model (3)-(4) is an approximation to the real edge. However, many observed profiles do not show easily discernible sharp edges in the presence of noise. In particular, red edges have the appearance of smooth transits between line and continuum. Blue edges are sharper, but are often accompanied by a trough at higher frequencies. Hence even in this case, the blue edge is often better described by the polynomial model than the non-linear model with its zero-continuum requirement. As a result the latter is seen to have large errors in most cases. However, when blue edges occur without a significant negative trough, the nonlinear model gives a better fit than the polynomial profile.

We have demonstrated through Monte Carlo experiments that we can obtain reasonable values for line edges and get good estimates of uncertainties. We checked that our technique is not sensitive to the functional form of the line profile, a test which indicates how robust our method is to the emissivity function of the disk and the energy-dependent detector response. Specifically, we verified that our fitting technique gives values of $g_{\min}$ and $g_{\max}$ that are not overly sensitive to the multiplication of the data by a smoothly varying, positive definite function. This procedure resulted in substantial changes in the variance of estimated roots. However, if the function does not change greatly in the vicinity of the edge, the new mean of Monte-Carlo simulations remained within the largest of the one σ-errors for the non-modified and modified data sets.

We also checked our method using two functions, one on either side of the best fit line edge, each giving a multiplicative factor which modifies the observed intensity, to vary both the line and the continuum independently. By choosing particular shapes for these function one can either augment or suppress the line with respect to the continuum data adjacent to the line. This mimics the effect of increasing or decreasing the emissivity of that part of the disk which contributes to the line edge. It turns out that multiplication by such a function can significantly change the error in the determination of the edge but the location of the

edge itself still remains within the largest of the one σ errors for the original and modified data. In the case where the line is suppressed and the tail of the line became very shallow, the error in the position of the edge increases. Conversely, highlighting the line and suppressing fluctuations in the continuum decreases the error.

These tests indicate that the Monte-Carlo method gives robust estimates of the position of the edge without great sensitivity to the details of the disk emissivity function. Certainly, there are limits. For example, if the disk is illuminated in an inhomogeneous fashion as a result of flares located close to the disk surface, the line contribution from a highly localized region of the disk could be mistaken for the red edge of the whole profile. In this case one would miss a faint red tail extending beyond this jump and get an overestimate of the inner extension of the accretion disk.

As discussed below, our Monte Carlo procedure worked poorly for estimating line edges in some particularly noisy data sets such as those of Iwasawa et al. (1996) for the Dark Minimum (DM) and Bright Flare (BF) states of MCG-6-30-15. The best fit for the red edge in DM data gives negative values for p_0, while the Monte-Carlo scattering of points around best fit for the red edge in BF data gives negative mean value of p_0 in sharp contrast with the best fit of 4.13 keV to the actual data points. To evaluate the position of the red edge in these noisy data sets we can formulate alternative methods for line edge detection which are based more directly on statistical properties of the line. For example, given a set of flux measurements as a function of energy, we could test the hypothesis that the fluxes are all consistent with continuum emission, using χ^2 to measure of goodness-of-fit (e.g., Bromley, Miller & Pariev 1998). An edge detection algorithm then might be to test the continuum hypothesis on the red-most channels, including successively bluer channels until the continuum hypothesis can be rejected at some specified level of confidence. The edge of the line would then identified with the energy of the bluest channel.

In principle, this "running χ^2" method is conservative. It requires only that enough channels be sufficiently different from the continuum that we can reject the continuum model. If the continuum were extremely well sampled, then possibly a sequence of outlying fluxes all packed at, say, the blue end of the set of channels could be dismissed as merely expected statistical fluctuations. A less conservative method should consider correlations between the fluxes in neighboring channels to enable a more sensitive edge detection.

A further drawback of the running χ^2 method is that it cannot distinguish between absorption and emission features. In practice, one can replace the flux in suspected absorption regions with exact continuum values or even randomly generated values. To down weight the effects of possible absorption features we also consider a "sign" statistic to estimate the likelihood that a set of fluxes contains a line edge. Specifically, we count the number of fluxes above and below the continuum and compare with the expected binomial distribution.

We applied both these methods to the line profile data and obtained limits on the red edge of the lines in the Iwasawa et al. (1996) Deep Minimum and Bright Flare data. The two methods yielded similar results (Figure 5), with the edge detected by the sign method being 10% bluer than that detected by the running χ^2 method.

3. Implications for MCG-6-30-15, NGC 4151, and NGC 3516 line profiles

3.1. MCG-6-30-15

MCG-6-30-15 is a nearby ($z = 0.008$) Seyfert 1 galaxy. The broad skewed iron line profile observed from this galaxy has drawn much attention from the X-ray community over the past few years after its discovery (Tanaka et al. 1995). Figure 2 shows the results of polynomial fitting for frequency extrema from different available observations of MCG-6-30-15. Figure 5 corresponds to the same profiles but fitted with the nonlinear edge detection procedure. Comparison of the edge estimates using the two different methods indicates that errors from the nonlinear fit are larger than errors from the polynomial fit (except in the "97b" data from Iwasawa et al. 1999, for which the nonlinear fit's error box is smaller than the error ellipse of the polynomial fit). Best fits with nonlinear method are, generally, very close to the Monte-Carlo mean values for the polynomial fits, with the exception of BF profile from Iwasawa et al. (1996). However, as we mentioned above, the nonlinear fitting of the BF data worked poorly, and the running χ^2 test gives somewhat redder position of the edge than polynomial fitting.

We reported briefly on the application of $g_{\min}$–$g_{\max}$ method in Bromley et al. (1998). The results for $g_{\min}$–$g_{\max}$ for Int, BF, and DM data of Iwasawa et al. (1996), reported in Bromley et al. (1998), were very conservative, i.e. the extent of both red and blue edges in Bromley et al. (1998) were probably underestimated. Our new edge detection procedure, which is designed to isolate an edge, not to find a bounding value, gives smaller $g_{\min}$ and larger $g_{\max}$. In contrast, the χ^2 rejection method used by Bromley et al. (1998) does not take into account correlations in positions of data points, thus it may miss extended emission edges which smoothly approach the continuum but at intensity levels which are comparable to the errors of observations. Our new fitting technique allows us to hone in on such significant edges, if they exist, although the uncertainties can be larger in this case. In choosing our new method over the χ^2 rejection technique, we are opting for precision over accuracy.

The "Int" data set gives the most restrictive point in the $g_{\min}$–$g_{\max}$ plane for determining the lower limit of the disk inclination angle. Using 2σ error limits for the position of that point results in the following absolute lower limits on i: in a thin-disk Schwarzschild system $i > 36°$ (nonlinear fitting, Fig. 5a) or $i > 38°$ (polynomial fitting, Fig. 2a); in an extreme Kerr system with a thin disk, $i > 34°$ (nonlinear fitting, Fig. 5c) or $i > 36°$ (polynomial fitting, Fig. 2c).

Incorporating all five available data sets, marked as T,97,97b,Int, and BF, one can estimate a likely lower bound on the inclination of a thin disk as $i > 44 \pm 6°$ (nonlinear), $i > 48 \pm 5°$ (polynomial) for a Schwarzschild system, and $i > 42 \pm 5°$ (nonlinear), $i > 45 \pm 5°$ (polynomial) for extreme Kerr system.

These results contradict the estimates of i obtained from the numerous fittings of the full line profile to thin-disk models: $30.2^{\circ+1.5}_{-2.7}$, $29.7^{\circ+2.9}_{-3.9}$ (Tanaka et al., 1995, Schwarzschild model), $26.8^{\circ+2.1}_{-1.0}$ (Tanaka et al., 1995, Kerr model), $29^{\circ+2.5}_{-3.2}$ (Dabrowski et al., 1997), $32^{\circ+2}_{-2}$ (Iwasawa et al., 1999). The most probable explanation for the discrepancy is that the blue edge of the profiles is not as sharp as predicted by the thin-disk models. The positions of the points in the frequency extrema diagrams for turbulent disk models (Figs. 2b, 2d, 5b, and 5d) indicate that the effects of finite disk thickness is to reduce the lower limit on the inclination of the disk. Smoothed blue wings are characteristic of turbulent disk profiles as well (Pariev & Bromley, 1998). Comparing Figs. 2a and 2b, 5a and 5b, one can see that the model of a thick disk around nonrotating black hole with the luminosity of $L \approx 0.5 L_{\rm ed}$ is enough to bring the lower bound on i from the position of the Int data point down to 30°. To reduce the most probable inclination estimate from the five data points (T,97,97b,Int,BF) to 30° requires higher accretion rates at a level of $L \approx L_{\rm ed}$. Since

the efficiency of converting energy to radiation is higher for an extreme rotating black hole, the effect of turbulent motions is smaller for the same values of L. By comparing Figs. 2c and 2d, 5c and 5d, one can see that at $L = L_{\rm ed}$ the absolute 2σ limit on i reduces to 30°, while one needs even higher accretion rates in order to diminish the most probable lower bound on i down to 30°. We thus conclude that the MCG-6-30-15 data suggest either a thin disk at relatively high inclination angle or a thick disk at lower inclination.

A key factor for our hypothesis that MCG-6-30-15 may harbor a thick disk is the mass of the black hole, since this determines the ratio of $L/L_{\rm ed}$. There is no compelling measurement of the mass of central black hole in MCG-6-30-15 to date. However, the form of the X-ray power density spectrum reported in Nowak & Chiang (1999) evidently is universal, spanning low mass ($\sim 10\,M_\odot$) objects like of Cyg X-1 to supermassive ($10^8\,M_\odot$) ones like NGC 5548. The scaling of the frequencies at which the power laws break led Nowak & Chiang (1999) to conclude that the mass of the black hole in MCG-6-30-15 is about $10^6\,M_\odot$, which is at the lower end of the supermassive black holes mass spectrum in AGNs (Richstone et al., 1998). Reynolds (2000) looked at possible reverberation delays between continuum emission in energy bands of 2–4 keV and 8–15 keV and emission in the 5–7 keV band containing the line in a long *RXTE* observation of MCG-6-30-15. He did not find any reverberation delays longer than 500 seconds. This result, along with X-ray variability data allowed him to conclude that the mass of the black hole is $\sim 10^6 - 10^7\,M_\odot$ in agreement with Novak & Chiang (1999) result. A multiwavelength study of MCG-6-30-15 (Reynolds et al., 1997) shows that the bolometric luminosity of the object is $\approx 8 \cdot 10^{43}\,{\rm erg\ s^{-1}}$. Thus, the mass of $10^6\,M_\odot$ implies that the accretion luminosity is roughly 60% of the Eddington luminosity. This estimate provides some grounds for the hypothesis that the extended edges of the line are caused by turbulence in an accretion disk.

If one believes that the luminosity of the accretion disk is 60% of the Eddington limit, one can conclude that the black hole in MCG-6-30-15 cannot rotate at the maximum rate, since disks around fast rotating Kerr black holes do not have turbulent velocities high enough to make a 30° inclination angle consistent with $g_{\rm max}$ for the "Int" data point. Together with the lower bound for a_* from the $g_{\rm min}$ values of the reddest observed line profiles (see below) this leads to the estimate of $a_* \approx 0.3$. It is interesting to point out that knowledge of the accretion disk luminosity can lead to a value of a_* from the position of the blue edge of the line. In the future, with improved understanding of the inner disk structure, one can hope to use the shape and position of the blue edge of the profile to obtain a better quantitative estimate of a_*.

Still, we cannot rule out that highly ionized regions of the disk, emitting iron lines at 6.7 keV and 6.97 keV, can also produce blue wing of the line. As seen in Figures 2 and 5, when the continuum was brighter (see the 97a data point from Iwasawa et al. 1999), the $g_{\rm max}$ was smaller than when the continuum was dimmer (97b data point). The data sets can be explained by asserting that in the 97a case the bright flare occurred close to the innermost region of the disk, and more distant regions of the disk were not sufficiently well illuminated to produce an extended blue wing. If highly ionized iron were skewing our inference of the blue edge, it would presumably do so in a manner that would be more noticeable during the bright flare. It does not seem that such a contribution spontaneously appears during the bright flare, since this would push the true $g_{\rm max}$ lower than we have measured, and the 97a data would then imply a lowered inclination angle bound which is inconsistent with the other datasets. In the absence of higher quality data, we can only say that contamination by a 6.7 keV line occurs in both cases or not at all.

The position of the Iwasawa et al. (1997) DM and the Iwasawa et al. (1999) 97a point in the $g_{\rm min}$–$g_{\rm max}$ diagram indicate that at the level of 2σ confidence there is emission coming from below $6R_g$, the innermost stable orbit of a Schwarzschild black hole. Figures 2 and 5 show that this conclusion is true regardless of the value of the black hole spin and thickness of the accretion disk. This can be considered as robust,

model-independent evidence that the central object in MCG-6-30-15 is emitting from regions in the strong gravitational field of a black hole. The most probable innermost radius of emission as determined by the 97a and DM points with an assumed inclination angle of 30° is 4–5R_g, and it is still within 6R_g for our higher inclination angle estimates. The location of the inner edge of the disk at these radii corresponds to the rotational parameter a_* to be in the range between 0.29 and 0.56. Since there is no significant iron absorption edge in the DM and 97a profiles, it is unlikely that any free-falling gas below innermost stable orbit can account for the observed extended red tails (Young, Ross, & Fabian, 1998). If the red tails of the DM and 97a profiles are produced by the emission of ionized iron, this will decrease $g_{\rm min}$ by a few per cent and make the estimates of the innermost radius of the disk even smaller and the rotational parameter a_* even higher. The caveat here is that we are able to determine only an upper bound for $g_{\rm min}$ of DM and the best nonlinear fit for 97a red edge falls close to the lower end of the error interval (Fig. 5, section 2). We could be missing extended red tails in the profiles as a result of large scatter and observational errors. Thus, it is reasonable to view our results for a_* as only a lower bound, i.e., that the black hole in MCG-6-30-15 rotates faster than about $a/M = 0.3$.

3.2. NGC 4151

NGC 4151 is a bright nearby ($z = 0.0033$) Seyfert 1.5 galaxy. It exhibits a broad Kα line profile very similar to the one observed in MCG-6-30-15 but with better signal-to-noise (Wang et al., 1999). The observed biconical geometry of the narrow line [O III] λ5007 region (Evans et al., 1993) suggests edge-on geometry of the accretion disk. The best estimate of the angle between axis of the emission line cone and line of sight is 65°. We may be tempted to adopt this value of inclination for the X-ray emitting disk as well, however, better constraints come from the geometry of the observed radio jet (Pedlar et al. 1993) which presumably originates in the inner region of the AGN. Unlike Evans et al. (1993), Pedlar et al. (1993) consider a geometry of the narrow line region in which the [O III] emission comes from a stripe where the ionization cone touches the galactic disk. This hypothesis is justified by a comparison of the velocities of the [O III] region and those of neutral hydrogen, which require the [O III] region to participate in the galaxy rotation and, thus be close to the plane of the galaxy. If the axis of the radio jet coincides with the axis of the ionization cone, then one can infer that the angle between the radio jet and the line of sight to be 40° (which turns out to be consistent with the observed relativistic beaming of $v = 0.15c$). Naturally, one expects the radio jet to be perpendicular to the plane of the inner part of the accretion disk where the collimation process occurs. This would then give an estimate of 40° for the inclination angle of X-ray emitting part of the accretion disk.

Our $g_{\rm min}$–$g_{\rm max}$ findings for NGC 4151 are plotted in Figures 1 and 4. The 2σ lower bound for the inclination angle of the disk derived from the thin disk model and a nonlinear edge fit (Fig. 4) is approximately 28°. The best-fit frequency extrema point in Fig. 4 gives a most probable inclination of 35°. The upper 2σ limit is 47°. All of these numbers are almost independent of value of a_*. Polynomial fitting (Fig. 1) gives somewhat larger values for $g_{\rm max}$; the corresponding results for the inclination angle are: the lower 2σ bound is 40°, best fit value is 48°, and the upper limit is 60°. The bounds differ by no more than 5° for different values of a_*. The line emission comes from a disk radius beyond 6R_g, with the most probable location of the innermost emission region at 8–10R_g. The turbulent disk model gives lower inclination angles and slightly (by approximately 1R_g) higher radii of the location of emissive spots.

Wandel, Peterson, & Malkan (1999) determine virial masses, emission-line region sizes, and the flux of ionizing continuum of AGNs using reverberation and photoionization techniques. For NGC 4151 they find

the mass of the black hole to be 1.2–2.2 $\cdot 10^7\, M_\odot$, the ionizing luminosity $5 \cdot 10^{42}$ erg s^{-1}, which corresponds to the ratio of ionizing luminosity to the Eddington luminosity as $3 \cdot 10^{-3}$. The ionizing luminosity is presumably comparable to the bolometric luminosity, since a large part of the AGN energy is expected to be radiated in the UV band. Thus, it is unlikely that the thickness of the disk has any effect on the iron line profile in NGC 4151.

Our analysis excludes the value of 65° for the inclination angle of the disk and is in good agreement with the value of 40° deduced by Pedlar et al. (1993). The unshifted main core of the line can be attributed to some relatively narrow line component whose origin is not the accretion disk. This component can be due to reflection of line photons from a surrounding torus and cool corona above the accretion disk (Poutanen et al. 1996).

3.3. NGC 3516

NGC 3516 is another close Seyfert 1 galaxy ($z = 0.009$) which is known to have a broad, skewed Kα iron line (Kriss et al., 1996; Nandra et al., 1997b; Nandra et al., 1997c; Nandra et al., 1999). We used the most recent observations by Nandra et al. (1999) for the application of our method. The $g_{\rm min}$-$g_{\rm max}$ point for the line profile for the whole observation (Fig. 1 in Nandra et al., 1999) as well as points for the line profile at each time interval (Fig. 3 in Nandra et al., 1999) were calculated. Figure 3 shows the results of polynomial fitting of lines edges, while Figure 6 represents the results of nonlinear fitting. One can see that the positions of the $g_{\rm min}$-$g_{\rm max}$ points obtained by these two different methods fall within each other's error boxes, though the errors of the nonlinear model are larger than polynomial fitting. To be conservative, we use the nonlinear fits (Fig. 6) in our analysis. From the position of points P2, P4, and P5 we conclude that the lower limit on the inclination angle of a thin Keplerian disk is $27 \pm 4°$. The best-fit locations in Fig. 6 indicate an inclination angle of the disk $43 \pm 4°$. These estimates are smaller for a rapidly rotating black hole but only by a few degrees.

We cannot put an upper limit on the inclination angle of the disk in this case. Nandra et al. (1999) fit an integrated state ("Int") profile and obtain the following values for the inclination of a thin disk: In the Schwarzschild model, $i = 35^{+1\,\circ}_{-2}$, and for the extreme Kerr model $i = 0^{+19\,\circ}$. We see that the appearance of blue wings in profiles P2, P7, and P4 causes our estimates of the inclination angle to increase compared to the fits from the integrated line profile. This discrepancy might be understood from Figure 1 of Nandra et al. (1999), showing that their fits for Schwarzschild and Kerr geometries have red wings which extend beyond the actual red edge of the line profile. Our determinations of the red edge of the Int profile give: linear fitting (Table 1) 3.53 ± 0.19 keV; nonlinear best fit (Table 2) 3.34 keV; and nonlinear fits to Monte-Carlo scattered points (Table 2) 3.98 ± 0.45. For the nonlinear fits we used only data points from channels 5 to 24, excluding the depression below 3.5 keV which is caused by absorption. For comparison, the fitting domain of Nandra et al. (1999) extends below 3 keV.

The inclination angle $i = 35^{+1\,\circ}_{-2}$ obtained by Nandra et al. (1999) for the Schwarzschild model is still consistent with our lowest limit, however, their estimate for the Kerr model is lower than any of our limits. Thus, our line edge determinations for time-resolved observations (P1-P8) favors a Schwarzschild black hole — the best fit to a Kerr model by Nandra et al. (1999) simply cannot account for blue wings of the line in P2, P4, and P5 time intervals. These transient blue wings may be caused, for example, by a temporary enhancement of irradiation of outer parts of the disk during the P2, P4, and P5 observation intervals. In the combined set of data, this enhancement of the blue wing gets averaged out and contributes to the

change (decrease) of the index of the best-fit power law model of the continuum.

NGC 3516 observations do not show a red tail as extended as in MCG-6-30-15. Large uncertainties in the data points in Fig. 6 prevent us from placing tight constraints on the radial location of the emitting region or from deriving any conclusions about the possible extent of the accretion disk below $6R_g$. The point with the lowest upper bound on $g_{\rm min}$ is P2. Using the square of errors for that point one can only conclude that the disk in NGC 3516 must be extended below $12R_g$ at a 2σ level of confidence, if one adopts $i = 35^\circ$ for the disk inclination.

Another possibility is that a thick disk model (Figs. 6b and 6d) could naturally explain the blue extended wings of the line without changing the fit to the core. Analysis of unevenly sampled X-ray luminosity data on NGC 3516 led Edelson & Nandra (1999) to obtain a rough estimate of the mass of the central black hole in NCG 3516 of $10^7\,M_\odot$. Infrared, optical and near UV fluxes from the NGC 3516 nucleus total $\approx 3 \cdot 10^{-10}\,{\rm erg\ s^{-1}cm^{-2}}$ (NASA/IPAC Extragalactic Database), while the far UV flux is $\approx 6 \cdot 10^{-11}\,{\rm erg\ s^{-1}cm^{-2}}$ (Goad et al. 1999), and the soft X-ray flux (NASA/IPAC Extragalactic Database) is $3 \cdot 10^{-12}\,{\rm erg\ s^{-1}cm^{-2}}$. This sums up to give a lower bound for the bolometric luminosity of $\approx 10^{44}\,{\rm erg\ s^{-1}}$ or the ratio $L/L_{\rm ed} \approx 0.08$.

If the above luminosity estimates are accurate, then the effects of turbulent broadening on the line profile are negligible. However, $L/L_{\rm ed}$ can be a few times larger, with the main uncertainty coming from poor knowledge of the mass of the central black hole. When results of reverberation studies for NGC 3516 become available, we hope to obtain a better estimate of the central black hole mass and to determine $L/L_{\rm ed}$ more accurately. Still, Figure 6d indicates that even a "maximally" thick disk with $L = L_{\rm ed}$ cannot make the Nandra et al. (1999) Kerr best fit value of $i = 0^{+19^\circ}$ to be consistent with $g_{\rm max}$ measurements for P2, P4, and P5 intervals (all the points of the curve $i = 19^\circ$ are below the error squares for P2, P4, and P5). In the case of a Schwarzschild model, comparison of Figs. 6a and 6b shows that the ratio of $L/L_{\rm ed} \approx 0.3$ is enough to raise the curve $i = 35^\circ$ such that it will be consistent with the best fit points for all observational intervals except P5 and P8. The inability of the Kerr thick disk model to account for the blue wings of the line strengthens our conclusion that the black hole in NGC 3516 should be rotating slowly

4. Summary

In this work we suggest a method which allows us to put bounds on the geometry and kinematics of the line emitting surface of a relativistic accretion disk around a supermassive black hole. Our technique is not sensitive to models of the illuminating source, the distribution of illuminating radiation over the disk surface, or the angular distribution of the reflected line in the rest frame of the reflecting material. We use our method to determine the positions of the red and blue edges of observed emission lines and extract information from these positions by comparison with the results of a fully relativistic ray-tracing code. The code generates maps of line-frequency extrema, and it can be used to demonstrate explicitly the differences which can arise as a result of black hole spin and turbulence in an accretion disk.

Conventionally, the only way to identify black hole rotation is to find emission from within the innermost stable orbit of a nonrotating black hole. Our method illustrates that if one has information about the geometry of the accretion flow from some other observation such as the inclination angle of a jet, along with an estimate of the luminosity relative to Eddington, then a new measure of the hole's spin may be available. We can thus break the "degeneracy" that exists between rotating and nonrotating black holes in a new way.

Certainly, our method cannot be a substitute for the fitting of the whole shape of the line assuming a particular emissivity law (power law axisymmetric in most works) and it cannot provide interesting information about the emissivity law itself. However, it can provide bounds on the geometry of the disk and the angular momentum of the black hole, which any emissivity model should satisfy. Therefore, it is important to emphasize the position of the line edges and to test model parameters obtained as a result of line profile fitting against the constraints provided by our method.

A drawback of the method are uncertainties in the determination of the position of the edges. A main focus of this paper is to find a reasonable edge detection algorithm to replace the conservative edge-boundary limits found by Bromley, Miller & Pariev (1998). We perform Monte-Carlo simulations of the data set using fits to the line edges with both a nonlinear sharp-edge model and a polynomial model which makes no a priori assumption about the shape of the line profile. We find reasonable agreement between models, both in terms of best-fit values and the error distributions.

Another drawback of the method is possible contamination with iron Kβ line, nickel Kα line, 6.7 keV and 6.97 keV Kα lines of highly ionized iron. We made corrections to profiles for the iron Kβ line using a Kβ-to-Kα yield ratio and for the nickel Kα line using a fiducial yield of 0.06 relative to iron Kα (see George & Fabian 1991). For quality of spectra currently available, these corrections are small.

We illustrate frequency extrema method by applying it to the Seyfert galaxies MCG-6-30-15, NGC 4151, and NGC 3516. The results for MCG-6-30-15 show that the commonly assumed inclination angle of 30° for a thin accretion disk is inconsistent with the position of the blue edge of the line at a 3σ level. The thick turbulent disk model can remedy this discrepancy, since it leads to appearance of a smooth blue wing in the line while the changes to the main profile are not so large (Pariev & Bromley, 1998). Recent estimates of the mass of the black hole in MCG-6-30-15 favor a luminosity ratio $L/L_{\rm ed} \sim 0.6$, which is enough to account for the $g_{\rm max}$ for all observations of the iron line in MCG-6-30-15 published to date. Furthermore, frequency extrema lead us to conclude that the black hole in MCG-6-30-15 must be rotating with at least $a/M = 0.26$.

For NGC 4151 our method excludes face on and edge on geometries, while giving bounds for the inclination angle of X-ray emitting inner disk of $50 \pm 10°$. These bounds are consistent with the models of the ionization cone grazing the disk by Pedlar et al. (1993) and two X-ray emitting disks of Wang et al. (1999). However, our bounds are not consistent with the $i = 65°$ geometry assumed by Evans et al. (1993) based on the observation of the biconical geometry of the narrow line [O III] λ5007 sources. Because of very low ratio of $L/L_{\rm ed}$, effects of turbulence in this source are negligible.

We find that frequency extrema results combined with line profile fitting by Nandra et al., (1999) favors Schwarzschild vs. Kerr model for NGC 3516. Although $L/L_{\rm ed} \sim 0.08$ for this source, the determination of the mass of the black hole is very uncertain. The possibility exists that the thick disk model may be relevant for NGC 3516 and could explain the blue wings of the line, observed during monitoring of this source by Nandra et al. (1999).

Further reverberation mapping results will provide better estimates of the mass of the black holes in nearby Seyferts and allow the thick turbulent disk model to have more predictive power for each individual source. Certainly, going beyond our simplifying assumptions and incorporating results of modeling of X-ray reflection spectra from the disk surface would be the next step to interpret higher quality spectral data from XMM and Constellation-X missions.

We are grateful to K. Nandra and J.-X. Wang for supplying us with the digital versions of iron line profiles. Many thanks go to S.A. Colgate for constant support and encouragement during work on this project. The comments of the referee improved presentation of this work. The SGI/Cray supercomputer used in this research was provided through funding from the NASA Offices of Space Sciences, Aeronautics, and Mission to Planet Earth. This research made use of the NASA/IPAC Extragalactic Database (NED), which is operated by the Jet Propulsion Laboratory, California Institute of Technology, under contract with NASA. Partial support from the NASA Astrophysics Theory Program and U.S. Department of Energy through the LDRD program at Los Alamos National Laboratory is also acknowledged.

REFERENCES

Agol, E., & Krolik, J.H. 2000, ApJ, 528, 161

Bardeen, J.M., & Peterson, J.A. 1975, ApJ, 195, L65

Beloborodov, A.M., Abramowicz, M.A., & Novikov, I.D. 1997, ApJ, 491, 267

Bromley, B.C., Chen, K., & Miller, W.A. 1997, ApJ, 475, 57

Bromley, B.C., Miller, W.A., & Pariev, V.I. 1998, Nature, 391, 54

Chen, K., & Halpern, J.P. 1989, ApJ, 344, 115

Cunningham, C.T. 1975, ApJ, 202, 788

Dabrowski, Y., Fabian, A.C., Iwasawa, K., Lasenby, A.N., & Reynolds, C.S. 1997, MNRAS, 288, L11

Edelson, R., Nandra, K. 1999, ApJ, 514, 682

Evans, I.N., Tsvetanov, Z., Kriss, G.A., Ford, H.C., Caganoff, S., & Koratkar, A.P. 1993, ApJ, 417, 82

Fabian, A.C., Iwasawa, K., Reynolds, C.S., & Young, A.J. 2000, PASP, 112, 1145

Fabian, A.C., Rees, M.J., Stellar, L., & White, N.E. 1989, MNRAS, 238, 729

George, I.M., & Fabian, A.C. 1991, MNRAS, 249, 352

Goad, M.R., Koratkar, A.P., Kim-Quijano, J., Korista, K.T., O'Brien, P.T., & Axon, D.J. 1999, ApJ, 524, 707

Iwasawa, K., et al. 1996, MNRAS, 282, 1038

Iwasawa, K., Fabian, A.C., Young, A.J., Inoue, H., Matsumoto, C. 1999, MNRAS, 306, L19

Kriss, G., et al. 1996, ApJ, 467, 629

Laor, A. 1991, ApJ, 376, 90

Lee, J.C., Fabian, A.C., Brandt, W.N., Reynolds, C.S., & Iwasawa, K. 2000, MNRAS, submitted

Luminet, J.-P. 1979, A&A, 75, 228

Magdziarz, P., & Zdziarski, A.A. 1995, MNRAS, 273, 837

Matt, G., Fabian, A.C., & Ross, R.R. 1993, MNRAS, 262, 179

Matt, G., Fabian, A.C., & Ross, R.R. 1996, MNRAS, 278, 1111

Matt, G., Perola, G.C., & Piro L. 1991, A&A, 247, 25

Mushotzky, R.F., Fabian, A.C., Iwasawa, K., Kunieda, H., Matsuoka, M., Nandra, K., & Tanaka, Y. 1995, MNRAS, 272, L9

Nandra, K., George, I.M., Mushotzky, R.F., Turner, T.J., & Yaqoob, T. 1997c, 476, 70

Nandra, K., George, I.M., Mushotzky, R.F., Turner, T.J., & Yaqoob, T., 1997a, ApJ, 477, 602

Nandra, K., George, I.M., Mushotzky, R.F., Turner, T.J., & Yaqoob, T. 1999, ApJ, 523, L17

Nandra, K., Mushotzky, R.F., Yaqoob, T., George, I.M., & Turner, T.J. 1997b, MNRAS, 284, L7

Novikov I.D., & Thorne K.S. 1973, in Black Holes, eds. DeWitt C., DeWitt B.S. (New York:Gordon and Breach), 343

Nowak, M.A., & Chiang, J. 1998, ApJ, 531, L13

Paczynski, B. 2000, submitted to ApJ, astro-ph/0004129

Page, D.N., & Thorne, K.S. 1974, ApJ, 191, 499

Pariev V.I., & Bromley B.C. 1998, ApJ, 508, 590

Pedlar, A., Kukula, M.J., Longley, D.P.T., Muxlow, T.W.B., Axon, D.J., Baum, S., O'Dea, C., & Unger, S.W. 1993, MNRAS, 263, 471

Poutanen, J., Sikora, M., Begelman, M.C., & Magdziarz, P. 1996, ApJ, 465, L107

Reynolds, C.S. 2000, ApJ, 533, 811

Reynolds, C.S., & Begelman, M.C. 1997, ApJ, 488, 109

Reynolds, C.S., & Fabian, A.C. 1997, MNRAS, 290, L1

Reynolds, C.S., Young, A.J., Begelman, M.C., Fabian, A.C. 1999, ApJ, 514, 164

Reynolds, C.S., Ward, M.J., Fabian, A.C., & Celotti, A. 1997, MNRAS, 291, 403

Richstone, D., et al. 1998, Nature, 395A, 14

Ruszkowski, M. 2000, MNRAS, 315, 1

Ruszkowski, M., & Fabian, A.C. 2000, MNRAS, 315, 223

Shakura, N.I., & Sunyaev, R.A. 1973, A&A, 24, 337

Tanaka, Y., et al. 1995, Nature, 375, 659

Thorne, K.S., 1974, ApJ, 191, 507

Wandel, A., Peterson, B.M., Malkan, M.A. 1999, ApJ, 526, 579

Wang, J.-X., Zhou, Y.Y., & Wang, T.-G. 1999, ApJ, 523, L129

Weaver, K.A., & Yaqoob, T. 1998, ApJ, 502, L139

Young, A.J., & Reynolds, C.S. 2000, ApJ, 529, 101

Young, A.J., Ross, R.R., & Fabian, A.C. 1998, MNRAS, 300, L11

Życki, P.T., & Czerny, B. 1994, MNRAS, 266, 653

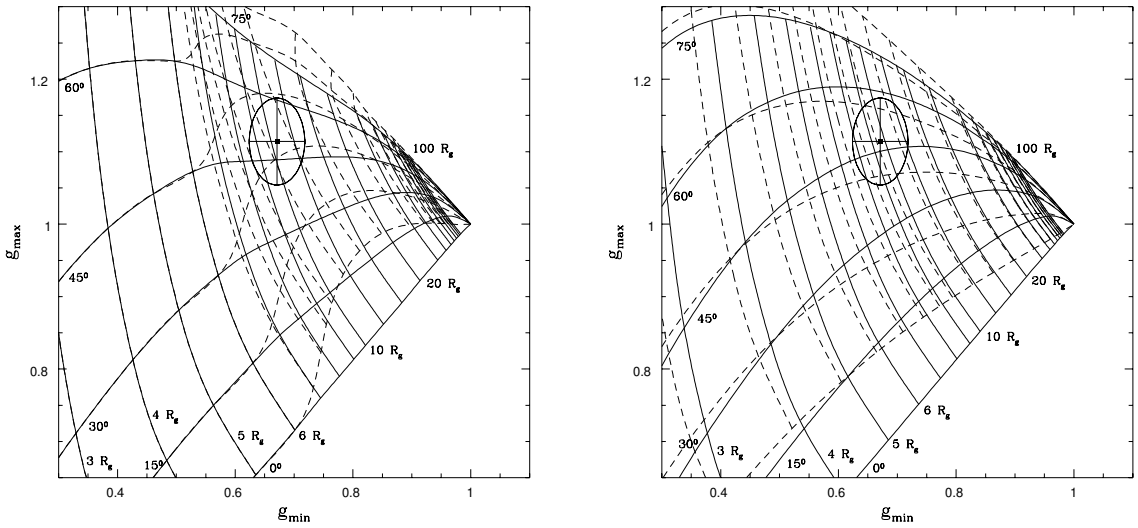

Fig. 1.— Maps of minimum and maximum redshifts for the case of Schwarzschild (a) and extreme Kerr (b) black holes. The grid of constant inclination angle (approximately horizontal lines) and equal radii (lines in vertical direction) are plotted. Solid lines correspond to the thin Keplerian disk model; dashed lines are for the turbulent thick disk model with Eddington luminosity $L = L_{edd}$. In the region with radii $r < 6R_g$ in the Schwarzschild case the gas was considered to be free-falling. The point is for NGC 4151 data by Wang et al. (1999). Error ellipse of polynomial fits is drawn at 2σ level contour. The scale on plots (a) and (b) is the same as well as on all g_{min}–g_{max} plots in this work.

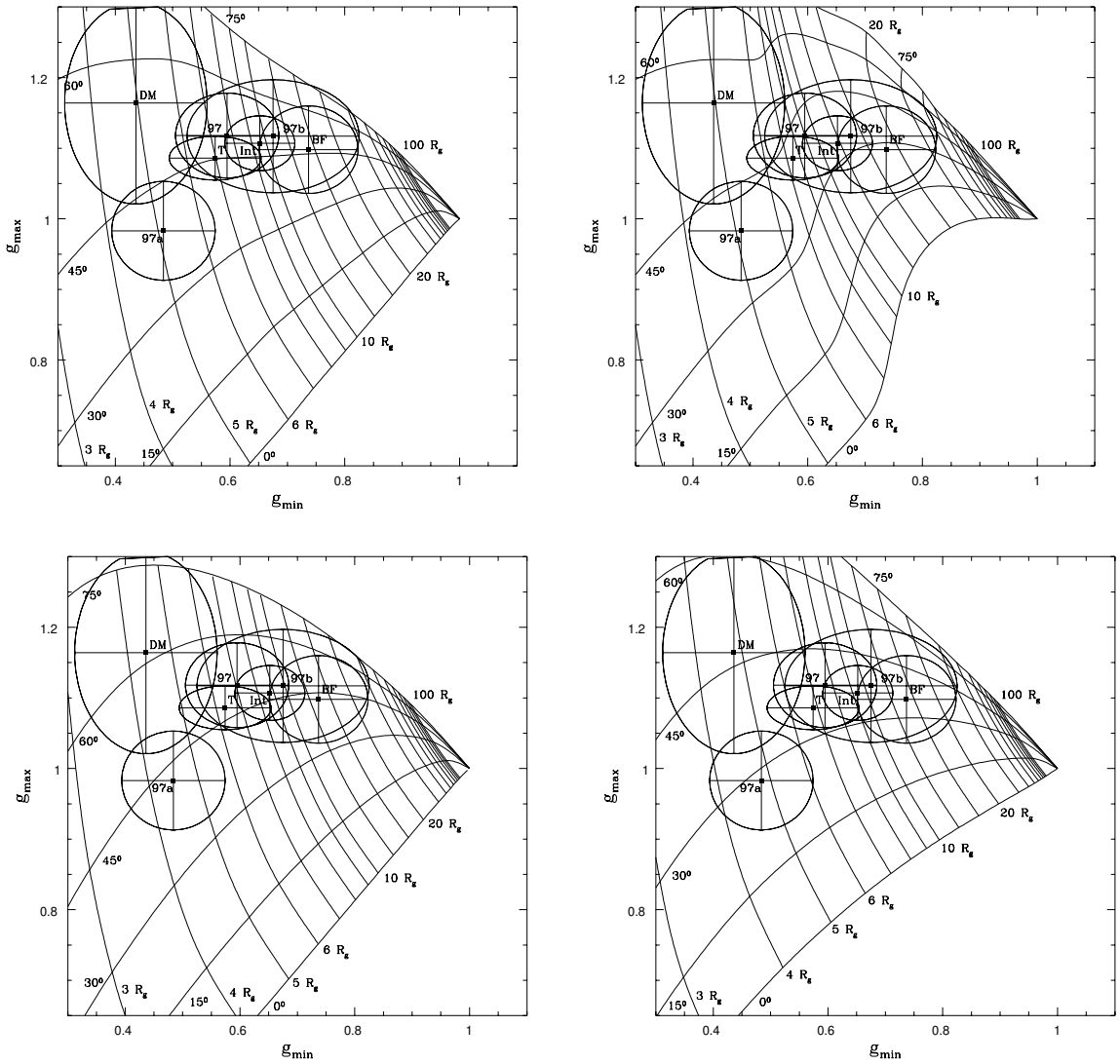

Fig. 2.— Data from MCG-6-30-15 plotted on a maximum and minimum frequency shift diagram. Error ellipses of polynomial fits are shown at a 2σ level contour. Observational data points on all four panels are the same. The point marked as T stands for the Tanaka et al. (1995) data. Int, BF and DM denote intermediate, bright flare and dark minimum spectra from Iwasawa et al. (1996). Points 97, 97a and 97b are for the average profile (97), bright flare subset (97a) and minimum subset (97b) from Iwasawa et al. (1999). The panels differ by the model used for the disk–black hole system. The top two panels are for a Schwarzschild black hole: Fig. (a) is for thin disk model, and Fig. (b) is for thick disk model. The bottom two panels are for extreme Kerr cases: Fig. (c) is for the thin disk model, Fig. (d) is for the thick disk model.

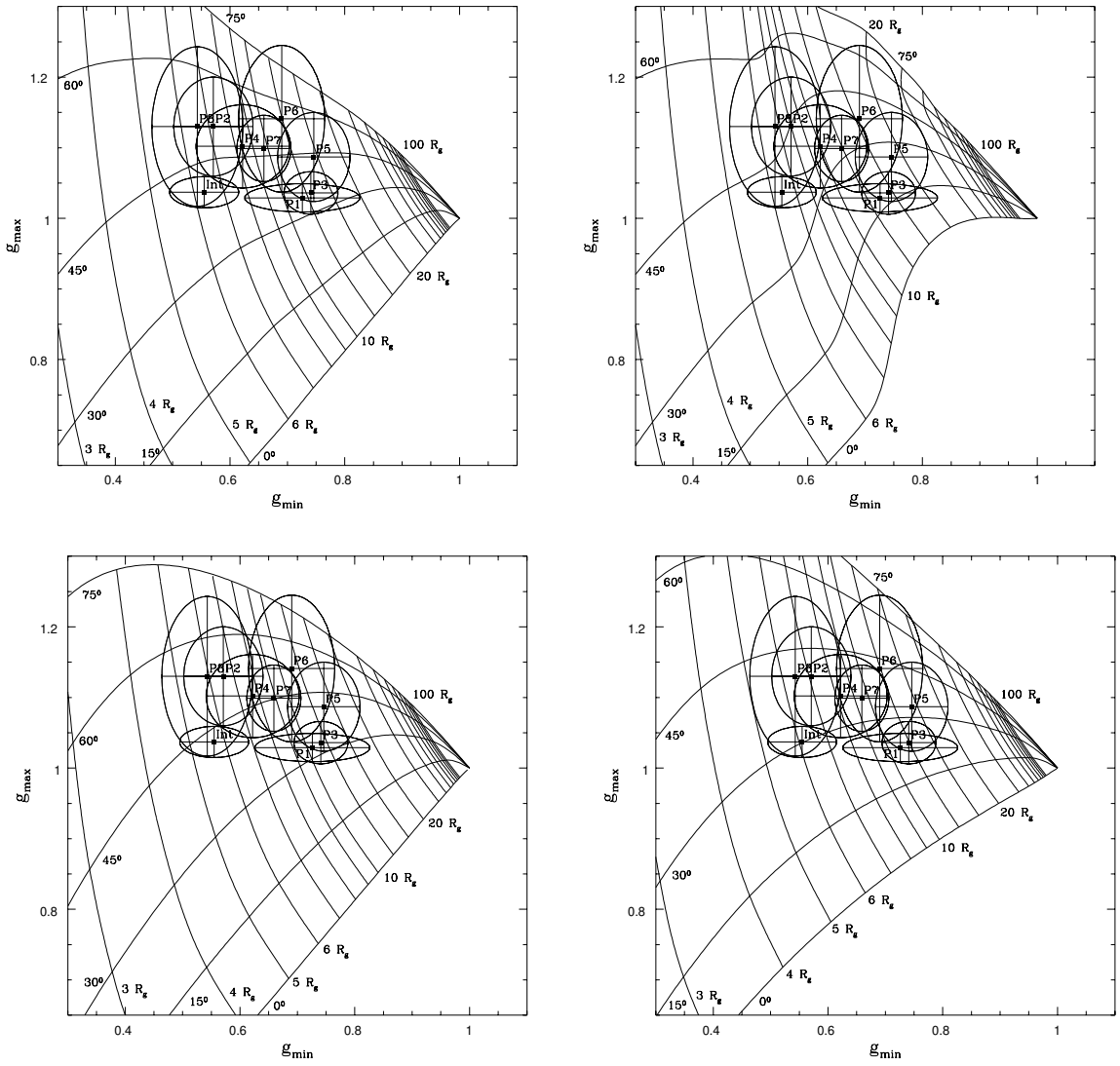

Fig. 3.— Data from NGC 3516 plotted on maximum and minimum frequency shift diagrams. Error ellipses of polynomial fits are shown at a 2σ level contour. Observational data are the same on all panels and are taken from Nandra et al. (1999). The point designated "Int" is for the profile integrated over the whole observation. Points designated "P1" through "P8" are for shorter time intervals of the observation. The panels differ by the model used for the disk–black hole system just as in Figure 2.

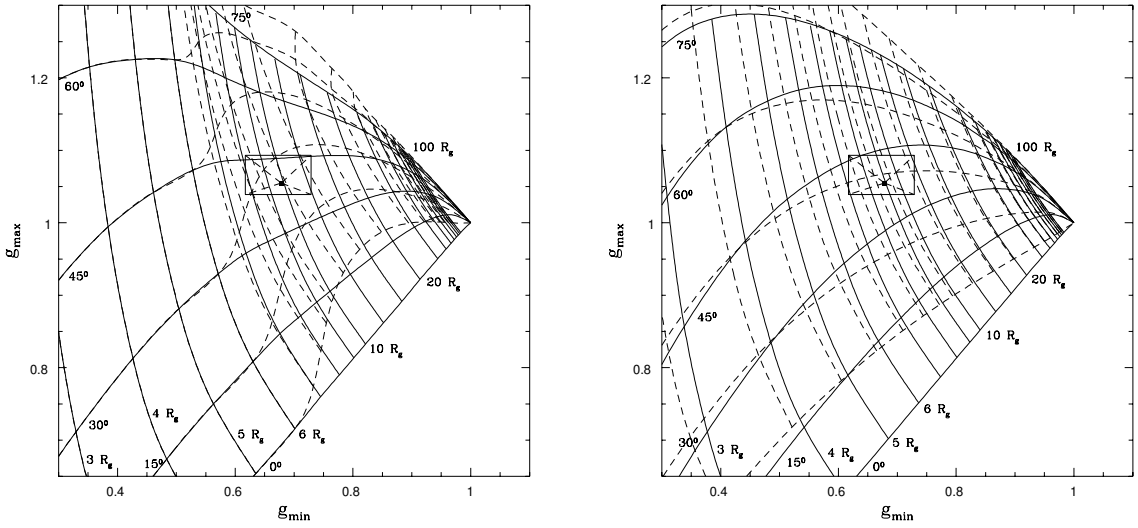

Fig. 4.— The results of continuum + line edge model fitting to the NGC 4151 data by Wang et al. (1999). All explanations and notations are the same as for Fig. 1 but using the non-linear "sharp edge" fitting model.

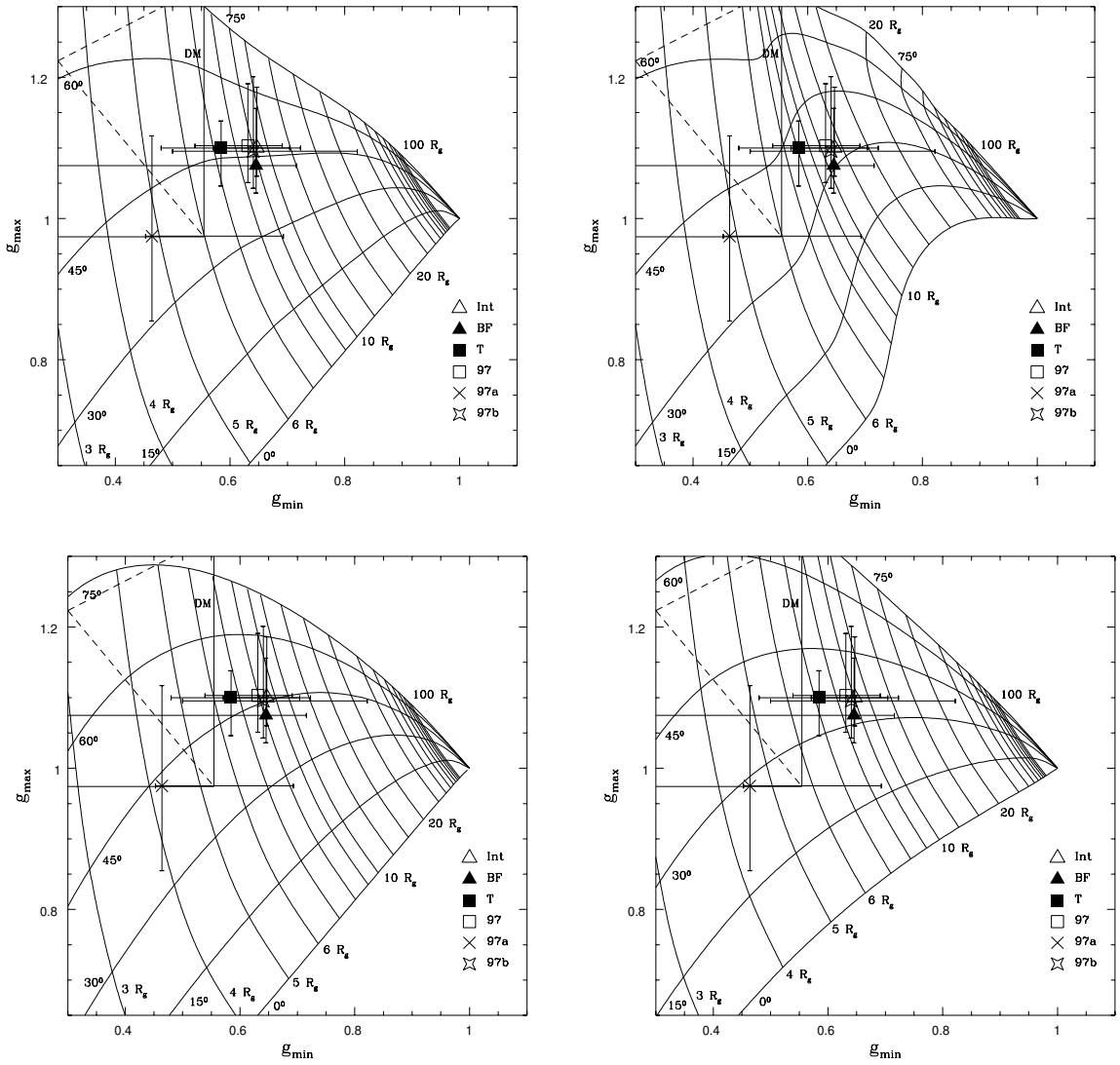

Fig. 5.— The results of continuum + line edge model fitting to the MCG-6-30-15 data. All explanations and notations are the same as for Fig. 2 but using the non-linear "sharp edge" fitting model. Only blue limits for the red edge in the case of DM and BF data are obtained.

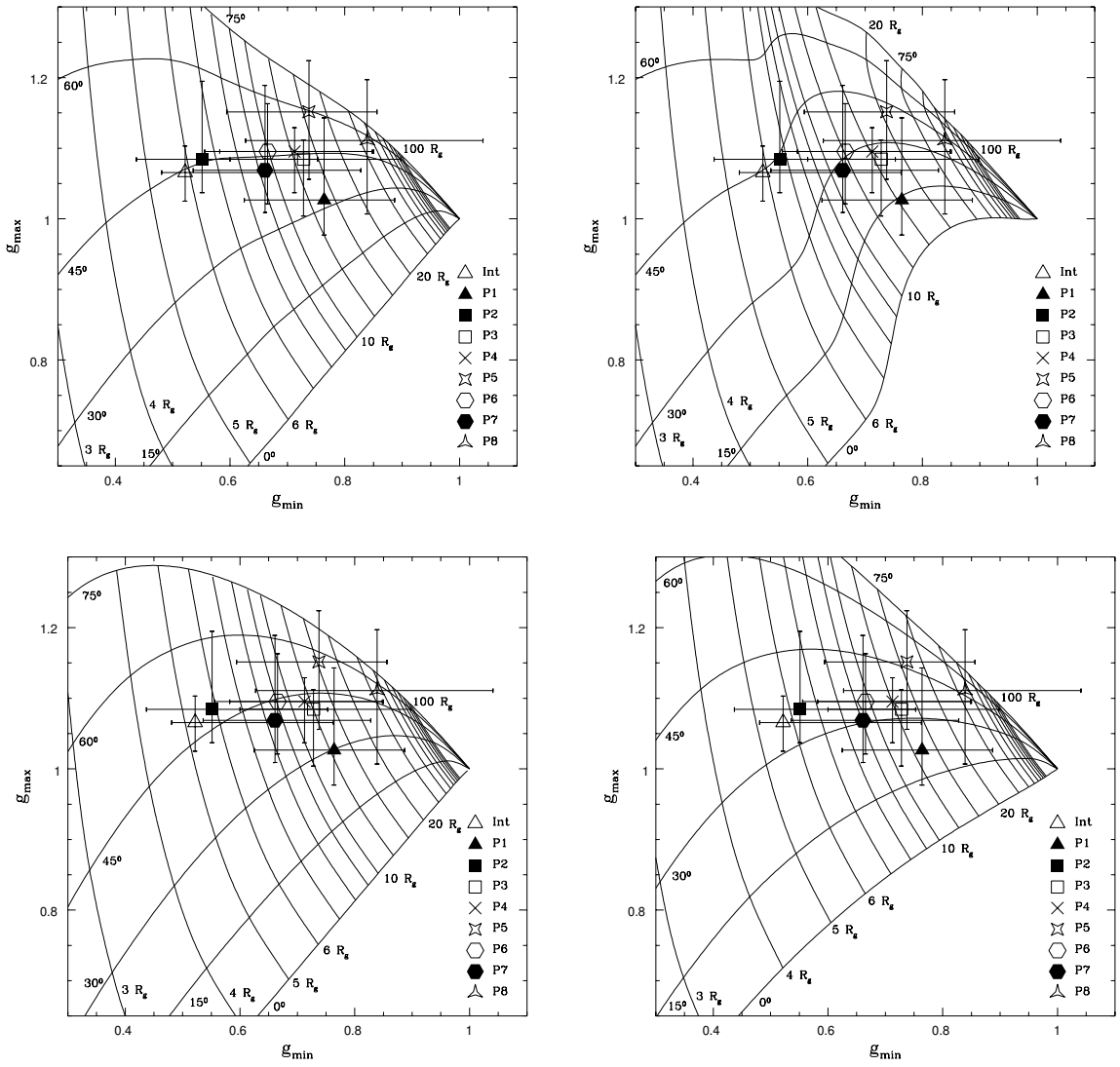

Fig. 6.— The results of continuum + line edge model fitting to the NGC 3516 data. All explanations and notations are the same as for Fig. 3 but using the non-linear "sharp edge" fitting model.

Table 1. Results of Fitting the Line Edges with Polynomial Model

Observation	Edge	Points	Approximation	keV	$g \pm 2\sigma$	χ^2/dof
Tanaka95	Red	1-16	quadratic, MC around actual data	3.67±0.25	0.57±0.08	···
Tanaka95	Blue	26-31	quadratic, MC around actual data	6.90±0.10	1.078±0.031	···
I96, Int	Red	1-29	cubic, MC around actual data	4.17±0.19	0.652±0.061	52.81/25
I96, Int	Blue	42-54	quadratic, MC around actual data	7.08±0.12	1.107±0.039	15.29/10
I96, BF	Red	1-32	quadratic, MC around actual data	4.72±0.28	0.737±0.086	66.58/29
I96, BF	Blue	35-45	cubic, MC around actual data	7.025±0.199	1.098±0.062	13.53/7
I96, DM	Red	1-22	cubic, MC around actual data	2.79±0.40	0.436±0.124	41.21/18
I96, DM	Blue	28-36	quadratic, MC around actual data	7.45±0.46	1.164±0.143	10.69/6
I99, Int	Red	1-6	quadratic, MC around actual data	3.79±0.30	0.59±0.09	···
I99, Int	Blue	20-24	quadratic, MC around actual data	7.12±0.17	1.11±0.06	···
I99, a	Red	1-33	quadratic, MC around actual data	3.07±0.29	0.48±0.09	···
I99, a	Blue	37-43	quadratic, MC around actual data	6.24±0.23	0.975±0.07	···
I99, b	Red	1-34	quadratic, MC around actual data	4.29±0.47	0.67±0.15	···
I99, b	Blue	37-41	quadratic, MC around actual data	7.09±0.26	1.108±0.08	···
NGC 4151	Red	6-15	quadratic, MC around actual data	4.28±0.15	0.669±0.047	···
NGC 4151	Blue	23-40	quadratic, MC around actual data	7.78±0.10	1.216±0.031	···
NGC 3516, Int	Red	1-19	quadratic, MC around actual data	3.53±0.19	0.55±0.06	···
NGC 3516, Int	Blue	36-39	quadratic, MC around actual data	6.58±0.07	1.028±0.022	···
NGC 3516, P1	Red	18-36	quadratic, MC around actual data	4.58±0.32	0.72±0.10	···
NGC 3516, P1	Blue	37-43	cubic, MC around actual data	6.51±0.07	1.02±0.02	···
NGC 3516, P2	Red	1-36	quadratic, MC around actual data	3.62±0.22	0.566±0.069	···
NGC 3516, P2	Blue	38-48	cubic, MC around actual data	7.14±0.23	1.12±0.07	···
NGC 3516, P3	Red	23-36	cubic, MC around actual data	4.70±0.15	0.734±0.047	···
NGC 3516, P3	Blue	38-41	quadratic, MC around actual data	6.57±0.095	1.027±0.030	···
NGC 3516, P4	Red	1-31	quadratic, MC around actual data	3.94±0.52	0.616±0.081	···
NGC 3516, P4	Blue	38-47	quadratic, MC around actual data	6.99±0.19	1.092±0.059	···
NGC 3516, P5	Red	1-30	cubic, MC around actual data	4.73±0.20	0.739±0.063	···
NGC 3516, P5	Blue	38-48	cubic, MC around actual data	6.89±0.20	1.077±0.063	···
NGC 3516, P6	Red	19-30	quadratic, MC around actual data	4.38±0.24	0.6844±0.075	···
NGC 3516, P6	Blue	39-48	quadratic, MC around actual data	7.24±0.33	1.131±0.103	···
NGC 3516, P7	Red	18-36	cubic, MC around actual data	4.18±0.15	0.653±0.047	···
NGC 3516, P7	Blue	38-46	quadratic, MC around actual data	6.97±0.15	1.089±0.047	···
NGC 3516, P8	Red	1-36	cubic, MC around actual data	3.44±0.25	0.538±0.078	···
NGC 3516, P8	Blue	40-48	quadratic, MC around actual data	7.17±0.36	1.120±0.112	···

Note. — MC is short for Monte-Carlo; I96 in the first column refers to the data from Iwasawa et al. (1996) for Intermediate (Int), Bright Flare (BF),and Deep Minimum (DM) data sets; I99 refers to the data from Iwasawa et al. (1999) for the whole observation (Int), for time intervals (a) and (b); Tanaka95 to the data from Tanaka et al. (1999); NGC 4151 data are from Wang et al. (1999); NGC 3516 data are from Nandra et al. (1999) for the mean line profile (Int) and for 8 time intervals (P1-P8); the last column contains χ^2 averaged over Monte-Carlo realizations.

Table 2. Results of Fitting the Line Edges with Nonlinear Model

Observation	Edge	Points	Approximation	keV	$g \pm 2\sigma$	χ^2/dof
Tanaka95	Red	1-16	linear, MC around actual data	3.79±0.36	0.592±0.112	35.26/14
Tanaka95	Red	1-16	linear, actual best fit	3.74	···	16.95/14
Tanaka95	Blue	26-34	quadratic, MC around actual data	6.99±0.15	1.092±0.046	15.96/6
Tanaka95	Blue	26-34	quadratic, actual best fit	7.04	···	8.37/6
I96, Int	Red	1-29	linear, MC around actual data	4.14±0.24	0.647±0.076	
I96, Int	Red	1-29	linear, actual best fit	4.14	···	25.50/27
I96, Int	Blue	42-56	quadratic, MC around actual data	7.20±0.21	1.123±0.063	
I96, Int	Blue	42-56	quadratic, actual best fit	7.04	···	5.01/12
I96, BF	Red	1-33	linear, MC around actual data	4.88±0.93	0.763±0.290	
I96, BF	Red	1-33	linear, actual best fit	4.13	···	43.71/31
I96, BF	Red	···	n-points χ^2 estimate[a]	4.58	···	···
I96, BF	Blue	34-45	quadratic, MC around actual data	7.02±0.19	1.096±0.060	
I96, BF	Blue	34-45	quadratic, actual best fit	6.88	···	6.05/9
I96, DM	Blue	28-36	linear, MC around actual data	7.37±0.57	1.152±0.178	···
I96, DM	Blue	28-36	linear, actual best fit	7.83	···	3.75/7
I96, DM	Red	···	n-points χ^2 estimate[a]	3.55	···	···
I99, Int	Red	1-7	quadratic, MC around actual data	3.94±0.24	0.615±0.076	5.91/4
I99, Int	Red	1-7	quadratic, actual best fit	4.04	···	0.83/4
I99, Int	Blue	20-25	quadratic, MC around actual data	7.17±0.22	1.121±0.070	5.16/3
I99, Int	Blue	20-25	quadratic, actual best fit	7.06	···	1.65/3
I99, a	Red	1-34	linear, MC around actual data	3.67±0.38	0.573±0.120	57.44/32
I99, a	Red	1-34	linear, actual best fit	2.97	···	23.45/32
I99, a	Blue	37-43	linear, MC around actual data	6.31±0.42	0.986±0.131	9.33/5
I99, a	Blue	37-43	linear, actual best fit	6.24	···	4.76/5
I99, b	Red	1-34	linear, MC around actual data	4.23±0.52	0.661±0.161	60.48/32
I99, b	Red	1-34	linear, actual best fit	4.10	···	25.74/32
I99, b	Blue	37-41	linear, MC around actual data	7.18±0.25	1.122±0.079	3.84/3
I99, b	Blue	37-41	linear, actual best fit	7.01	···	0.800/3
NGC 4151	Red	1-15	linear, MC around actual data	4.31±0.18	0.673±0.056	56.77/13
NGC 4151	Red	1-15	linear, actual best fit	4.34	···	17.35/13
NGC 4151	Blue	23-40	quadratic, MC around actual data	6.82±0.087	1.066±0.027	67.65/15
NGC 4151	Blue	23-40	quadratic, actual best fit	6.75	···	20.73/15
NGC 3516, Int	Red	5-24	linear, MC around actual data	3.98±0.45	0.622±0.141	81.33/18
NGC 3516, Int	Red	5-24	linear, actual best fit	3.34	···	27.54/18
NGC 3516, Int	Blue	34-45	linear, MC around actual data	6.81±0.13	1.064±0.039	41.72/10
NGC 3516, Int	Blue	34-45	linear, actual best fit	6.82	···	16.26/10
NGC 3516, P1	Red	18-36	linear, MC around actual data	4.83±0.42	0.756±0.131	51.67/17
NGC 3516, P1	Red	18-36	linear, actual best fit	4.89	···	21.51/17
NGC 3516, P1	Blue	38-48	linear, MC around actual data	6.78±0.27	1.060±0.083	16.68/9
NGC 3516, P1	Blue	38-48	linear, actual best fit	6.57	···	3.85/9

Table 2—Continued

Observation	Edge	Points	Approximation	keV	$g \pm 2\sigma$	χ^2/dof
NGC 3516, P2	Red	1-36	linear, MC around actual data	3.81±0.50	0.595±0.158	96.05/34
NGC 3516, P2	Red	1-36	linear, actual best fit	3.53	···	30.98/34
NGC 3516, P2	Blue	37-48	linear, MC around actual data	7.14±0.25	1.116±0.079	21.62/10
NGC 3516, P2	Blue	37-48	linear, actual best fit	6.94	···	6.13/10
NGC 3516, P3	Red	23-36	linear, MC around actual data	4.79±0.48	0.749±0.149	27.89/12
NGC 3516, P3	Red	23-36	linear, actual best fit	4.66	···	4.86/12
NGC 3516, P3	Blue	37-48	quadratic, MC around actual data	6.77±0.17	1.058±0.054	19.78/9
NGC 3516, P3	Blue	37-48	quadratic, actual best fit	6.94	···	5.07/9
NGC 3516, P4	Red	13-31	linear, MC around actual data	4.50±0.47	0.703±0.147	41.52/17
NGC 3516, P4	Red	13-31	linear, actual best fit	4.56	···	10.67/17
NGC 3516, P4	Blue	37-48	quadratic, MC around actual data	6.93±0.147	1.083±0.046	23.96/9
NGC 3516, P4	Blue	37-48	quadratic, actual best fit	7.01	···	10.74/9
NGC 3516, P5	Red	1-30	quadratic, MC around actual data	4.64±0.42	0.725±0.131	76.6/27
NGC 3516, P5	Red	1-30	quadratic, actual best fit	4.72	···	25.65/27
NGC 3516, P5	Blue	38-48	linear, MC around actual data	7.29±0.27	1.140±0.084	21.48/9
NGC 3516, P5	Blue	38-48	linear, actual best fit	7.37	···	8.42/9
NGC 3516, P6	Red	1-30	linear, MC around actual data	4.58±0.42	0.715±0.133	77.86/28
NGC 3516, P6	Red	1-30	linear, actual best fit	4.26	···	27.93/28
NGC 3516, P6	Blue	38-48	quadratic, MC around actual data	6.99±0.23	1.092±0.071	15.68/8
NGC 3516, P6	Blue	38-48	quadratic, actual best fit	7.01	···	4.26/8
NGC 3516, P7	Red	1-36	linear, MC around actual data	4.36±0.47	0.682±0.146	98.34/34
NGC 3516, P7	Red	1-36	linear, actual best fit	4.23	···	36.99/34
NGC 3516, P7	Blue	38-48	quadratic, MC around actual data	7.03±0.29	1.099±0.090	17.32/8
NGC 3516, P7	Blue	38-48	quadratic, actual best fit	6.84	···	6.16/8
NGC 3516, P8	Red	1-37	quadratic, MC around actual data	5.33±0.66	0.834±0.207	100.5/34
NGC 3516, P8	Red	1-37	quadratic, actual best fit	5.37	···	40.96/34
NGC 3516, P8	Blue	39-47	quadratic, MC around actual data	7.05±0.30	1.102±0.095	15.00/6
NGC 3516, P8	Blue	39-47	quadratic, actual best fit	7.11	···	6.77/6

[a]Blue conservative limit on the red edge from the n-points χ^2 rejection method

Note. — MC is short for Monte-Carlo; I96 in the first column refers to the data from Iwasawa et al. (1996) for Intermediate (Int), Bright Flare (BF),and Deep Minimum (DM) data sets; I99 refers to the data from Iwasawa et al. (1999) for the whole observation (Int), for time intervals (a) and (b); Tanaka95 refers to the data from Tanaka et al. (1999); NGC 4151 data are from Wang et al. (1999); NGC 3516 data are from Nandra et al. (1999) for the mean line profile (Int) and for 8 time intervals (P1-P8); the last column contains χ^2 averaged over Monte-Carlo realizations.